Investigations into the Removal of Micro-Particles from Surfaces Using Ultrafast Lasers

Investigations into the Removal of Micro-Particles from Surfaces Using Ultrafast Lasers

By

TIMOTHY JUSTIN LAMPMAN

A Thesis

Submitted to the School of Graduate Studies

in Partial Fulfillment of the Requirements for the Degree

Master of Applied Science

McMaster University

September 2002

MASTER OF APPLIED SCIENCE (2002) McMASTER UNIVERSITY
(ENGINEERING PHYSICS) Hamilton, Ontario

TITLE: Investigations into the Removal of Micro-Particles from Surfaces using Ultrafast Lasers

AUTHOR: Timothy J. Lampman
B.Sc. (University of Guelph)
M.Sc. (McMaster University)

ADVISOR: Professor Harold Haugen

PAGES: xii, 108

Ring the bells
That still can ring
Forget your perfect offering
There is a crack in everything
That's how the light gets in

Anthem, Leonard Cohen

Abstract

This thesis reports on the work performed on the manipulation of micro-particles on substrate surfaces using short laser pulses. For particles with diameters on the order of microns, the binding forces to surfaces are significantly larger than gravitational forces. To overcome these binding forces and manipulate the particles the use of femtosecond laser pulses has been investigated. Individual micro-particles (poly-divinylbenzene, glass and silver materials) with diameters around 2 μm were removed from substrate surfaces (dielectric, semiconductor and metal substrates) using a Ti:Sapphire laser system. The pulses produced at 800 nm had pulse lengths around 140 fs and were tightly focussed onto the surface using 5x and 10x microscope objectives. The peak fluence thresholds for particle removal were determined and the surfaces examined after irradiation by a scanning electron microscope and atomic force microscope to check for damage. The experimental results indicate that ablation of the substrate below the micro-particles is most likely to be responsible for micro-particle removal from the substrate surface when using femtosecond pulses. Ablation pits were observed for the dielectric micro-spheres on semiconductor substrates. It is also believed that ablation is responsible for the removal of other types of micro-particles from various substrates. Unlike the dielectric micro-sphere on semiconductor substrate results, the other particle–substrate combinations show a close correspondence between the removal and substrate ablation thresholds. It is believed that these results indicate the occurrence of ablation leading to the removal of the micro-particles. Calculations of the local electromagnetic fields around the micro-particles have also been carried out and the distributions used to interpret the experimental results.

Acknowledgments

A special thanks certainly goes to my supervisor, Dr. Harold Haugen. It was through his guidance, enthusiasm and infinite patience that this body of work saw its completion. I would also like to thank the rest of the past or present members of the Haugen lab: Jan Thøgersen for his initial efforts and research related to this project; Andrzej Borowiec for use of his experimental setup and help operating the laser; Henry Tiedje for his Paul trap, help in the lab and useful discussions; Qiang Liu for the metal substrates and information of metal and dielectric ablation thresholds; André Merizzi for useful discussions and further research into the topic of this thesis; and generally, everyone else in the lab for creating an interesting environment. Some of the research staff associated with the Brockhouse Institute for Materials Research also deserve an appreciation for their help with sample preparation and analysis. I am also indebted to the Department of Engineering Physics at McMaster University for their support and patience throughout this project.

I would also like to thank Natalia Kaniuk and Ma and Pa Lampman. No amount of words can describe what they have done for me.

Contents

List of Figures

List of Tables

Chapter 1

Introduction

The use of ultrafast lasers is on the rise in technological applications. Although femtosecond lasers have been around since the 1980's, they have mainly been used in scientific research applications. But it may be argued that this is starting to change due to the decrease in their purchase cost. They are also starting to become more compact—a necessary condition for most technical applications. As time moves along these current trends are expected to continue and before long, the ultrafast laser just might become an essential component of our society.

One of the big advantages of very short light pulses (ultrafast lasers produce picosecond or femtosecond pulses of light) is the strong electromagnetic field that is intrinsic to the pulse. Part of the attractiveness of this is that the strong fields exist while minimizing the pulse energy. Another benefit of short light pulses is that they allow for high time-resolution studies. This is an obvious advantage for scientific studies. For example, since one of the easiest ways known to interact with atoms or molecules is through light, ultrafast laser pulses have been used to study atoms and molecules in high-field regimes as well as on the time scale of some inter-atomic processes. The industrial applications of ultrafast lasers are also becoming noticed and an example of one application is *laser micro-machining* [1]. In this

application ultrafast lasers are used to etch—or in some cases, cut—a variety of materials for a variety of purposes. There certainly exist other applications (which include high resolution non-linear microscopy, imaging in scattering media and X-ray generation [2, 3]) and this work has examined some details surrounding one of them.

In the current initiative the application that was investigated was, in the most general terms, the micro-manipulation of particles with light. This is a broad term that could encompass optical trapping [4, 5], micro-particle modification [6], micro-patterning [7] or laser cleaning of surfaces [8, 9], to name a few applications. While the desired outcomes of such applications may vary, there is one common aspect: the interaction of the light fields with the particles and surrounding materials. To further introduce the background behind this work, the laser cleaning application will be discussed in a bit more detail. This application involves many different methods of cleaning, but the process of dry laser cleaning (DLC) is most relevant to the current work. In this process short laser pulses are used to irradiate contaminated surfaces with the desired result of contamination removal and clean substrate surfaces. This process involves cleaning the surfaces without any form of pre-processing and is different from a similar technique called wet laser cleaning where a fluid is applied to the surface prior to irradiation. A variety of types of lasers have been used to remove contamination from surfaces under dry conditions. This was purported to have been done without damaging the surface and can clean a surface in a relatively short amount of time (the laser beam is just scanned or rastered across the surface). Another advantage of using lasers to clean surfaces is that they could prove to be effective in removing very small particle contamination (particles with diameters of nanometers and several micrometers have proven to be hard to remove using certain cleaning techniques). These micro-particles are very hard to remove due to strong

binding forces and the smaller the particles get, the stronger the binding forces become relative to other forces which could act to remove the particles. This means that smaller particles are harder to remove from surfaces. Therefore, to remove the particles high intensities are needed while keeping the power delivered to the surface down so as not to heat it beyond its melting point. In the early 1990's the use of nanosecond lasers was initially investigated in laser cleaning and, given the current rate of development of ultrafast lasers, our thoughts were whether shorter pulses offer any advantages over longer nanosecond pulses. Therefore, one motivation behind this work was born.

In more specific terms, the research has focussed on the removal of micro-particles from a variety of types of material surfaces using femtosecond laser pulses. One obvious question pertained to the cause of the removal of micro-particles from the surface. Is it purely a result of the pulse's electromagnetic field, or something else? This essentially contains the main motivation behind this work; probing of the properties and effects of high intensity electromagnetic fields around micro-particles. In order to simplify the electromagnetic field distribution it was only the removal of single micro-particles that were examined. This was chosen to eliminate more complicated particle–particle interactions. The targeting of individual micro-particles was not only of interest to the electromagnetic field distributions, it also allowed for a good definition of the peak threshold pulse fluence required to remove micro-particles from surfaces, which may be of interest in several applications. In this same regard, the micro-particles used were actually spheres (when it was possible to find micro-spheres) so the particle geometry would be well-defined. After irradiation the surfaces were also examined to determine if there was any damage to the surface, or if there were other features on the surface. It was in this manner that the nature of the

interaction between ultrashort laser pulses and micro-particles could be examined.

This thesis will first cover some theoretical aspects of the reported work. In Chapter 2 several binding forces will be discussed. This chapter also presents several possible processes or mechanisms that may be responsible for micro-particle removal from surfaces using short laser pulses. Another important aspect of this work is the distribution of the electromagnetic field around the micro-particles. The methods used to calculated this are discussed in Chapter 3 as well as some of the general properties of the fields. Chapter 4 then discusses the experimental methods and equipment that was used and Chapter 5 follows up with a presentation of the experimental results for the variety of micro-particle/substrate materials used. It is then in Chapter 6 that the results of the research presented are combined to give an overview of the findings. There also remains many unanswered questions and, therefore, future research that could be performed. This is also discussed in the final chapter of this thesis.

Chapter 2

Micro-Particle Binding and Removal

Every complete scientific investigation should contain two basic components: a theoretical explanation and experimental verification. They are certainly complimentary; experimental data should be referenced with models to be explained and theory without experimental verification may simply be an artifact of logical reasoning with no real applicability. It is in this section that the theories of micro-particle binding and removal are presented. Several theories of binding and removal have been presented and all are not expected to play a significant role in the current work. Should the parameters that were explored in the current work be expanded on, these theories and their related forces may become significant.

In this chapter the binding forces between the micro-particle and substrate surface are presented first along with a discussion of their magnitudes. Then several of the possible mechanisms in which light can interact with the particle and substrate are considered and again, this is followed by a discussion of their magnitudes. These mechanisms have been termed *removal mechanisms* since they have been presented in terms of their ability to remove particles from surfaces. But they may be useful in other ways.

2.1 Binding Forces

The attraction between particles and surfaces can be surprisingly large. Most people are familiar with annoying attraction between Styrofoam packing pellets and just about everything around them. It seems that whenever one tries to stop them from sticking to everything, nothing seems to work (including gravity). In this case the binding force between the pellets and the object is due to electrostatic charge forces. This is one of the three main types of particle–surface binding forces. The other two forms are capillary forces and van der Waals forces. While other forms of binding forces may exist, such as chemical bonding between the particle and substrate [10], they are situations that would be specific to the materials used—and in some cases they could possibly result in significant forces—and because of this only the general forces will be discussed.

While the binding of the Styrofoam pellets is annoying, we can be thankful that their size is not much smaller since particles become harder to remove from surfaces as their size decreases. The magnitude of binding forces is proportional to either the radius, or the radius squared of the particle. In contrast, the force due to gravity is proportional to the radius cubed. Therefore, as the particle decreases in size the relative magnitude of the binding becomes quite large and for sufficiently small particles, the role gravity plays when considering forces acting on micro-particles is insignificant. Which type of binding force is actually the dominant force does depend on a variety of parameters. In the following sections a discussion of gravitational force and the three binding forces is presented. The theoretical treatment of the binding forces presented mainly comes from the work of R.A. Bowling [10] and in this chapter all parameters and equations are in SI units unless otherwise stated.

2.1.1 Gravitational Force

The force of gravity acting on the micro-particle has traditionally not been viewed as a binding force *per se.* However, if the substrate were located directly below the particle, one could argue that gravity is acting as a binding force since it would be pushing the particle onto the substrate. This argument is reversed if the substrate were directly above the particle; then gravity would act to remove the particle from the substrate. If the substrate were located somewhere between these two situations, gravity would act as a combination of both binding and removal forces. While the geometrical orientation of this force does not make it a real binding force, it does give a good yardstick to appreciate the magnitude of binding forces. The force due to gravity is given as

$$F = mg = \frac{4}{3}\pi\varrho a^3 g = \frac{\pi}{6}\varrho g d^3, \tag{2.1}$$

where ϱ is the density of the particle, g is the gravitational constant and a and d are the radius and diameter of the particle, respectively. We now look at binding forces that could play a larger role in keeping the micro-particles on the substrate surface.

2.1.2 Van der Waals Force

The classical view of an electrically neutral solid is that the electrons are bound to a well defined ground state and there exist no electromagnetic fields in the solid. However, due to our knowledge of quantum mechanics, this is not the whole picture. The electrons in the solid's constituent atoms or molecules can actually "jump" between multiple states. These excitations occur very rapidly as the time scale is governed by the Heisenberg uncertainty relationship. The result of this is that rapidly varying local electromagnetic fields are created in the solid which, when another solid is brought in close proximity to the first, leads to an attractive force called the van der Waals

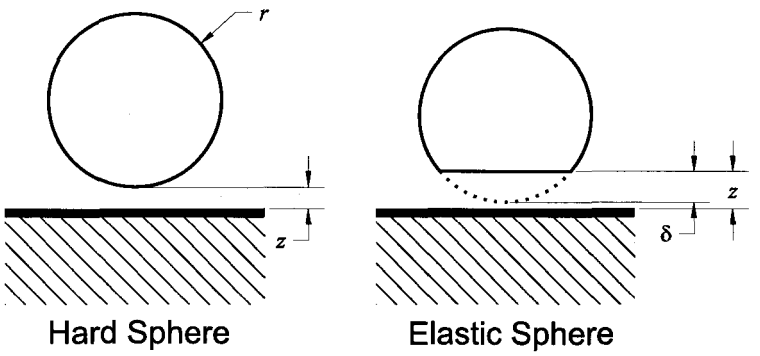

Figure 2.1: Parameters involved in the van der Waals binding force calculation. The situations for non-deformed spheres (Hard Sphere) and deformed spheres (Elastic Sphere) are shown.

force. In developing a mathematical theory behind this force two approaches have been used. The first is the microscopic approach which is commonly associated with the work of de Boer [11] and Hamaker [12]. In this approach the van der Waals force is calculated by first determining the van der Waals interaction between two isolated constituent atoms or molecules of the solid. This interaction is then integrated over the whole solid to determine the material van der Waals force. The microscopic approach is seen to have several drawbacks that limit its accuracy [13]. When the atoms or molecules are condensed into a solid their properties may significantly change such that the van der Waals interaction between two isolated components becomes a poor approximation. As well, this approach does not take into account the mobility of charge in the solid.

The second and more accurate method of determining the van der Waals force is the macroscopic approach of Lifshitz [14]. This considers the local polarizations in the material which lead to the attractive force. According to Lifshitz, the van der Waals force per unit surface area between two flat, parallel surfaces can be exactly calculated to be

$$\frac{F_{para}}{cm^2} = \frac{h}{8\pi^2 z^3}, \tag{2.2}$$

where h is the Lifshitz-van der Waals constant and z is the sphere–substrate surface separation (as shown in Figure 2.1). The attraction between a sphere and a flat surface cannot be calculated exactly, but with the help of the microscopic approach an approximate result can be found. In the microscopic approach the van der Waals force between two flat, parallel surfaces is given as

$$\mathcal{F}_{para} = \frac{A}{6\pi z^3}, \tag{2.3}$$

where A is the Hamaker constant. The result for a sphere and flat surface is given as

$$\mathcal{F} = \frac{Aa}{6z^2}. \tag{2.4}$$

The ratio of the two results is

$$\frac{\mathcal{F}}{\mathcal{F}_{para}} = \pi z a. \tag{2.5}$$

Based on the assumption that the microscopic approach predicts this ratio fairly accurately, the van der Waals force between a sphere and flat surface can be approximated by

$$F = \frac{ha}{8\pi z^2}. \tag{2.6}$$

Equation (2.6) shows that for a given material combination the van der Waals force depends on the radius of the sphere and the separation between the sphere's surface and the substrate surface. Area of contact is also an important parameter which has not be specifically included in Equation (2.6). If the materials are sufficiently elastic then deformations at either surfaces can become a significant factor in determining the force. The correction due to deformation of the particle is given as

$$F_{defm} = \frac{h\rho^2}{8\pi z^3}, \tag{2.7}$$

where ρ is the radius of the deformed area of the particle. The radius of deformation

of the particle has been proposed by Derjaguin *et al.* to be [15, 16]

$$\rho^3 = \frac{3}{4} P^o \left(\frac{1 - \sigma^2}{E} \right) a, \tag{2.8}$$

where σ and E are the Poisson ratio and Young's modulus of the particle respectively and P^o is the initial force prior to deformation. Using the van der Waals force from Equation (2.6) as the initial force the radius becomes

$$\rho^3 = \frac{3h}{32\pi z^2} \left(\frac{1 - \sigma^2}{E} \right) a^2. \tag{2.9}$$

A key parameter in the determination of the van der Waals force is the distance of separation between the surfaces. The distance may vary between different materials used but the standard generalized value in the literature is 4 Angstroms. Combining Equations (2.6) and (2.7) as well as taking a 0.4 nm surface separation, the total van der Waals force is

$$F_{vdW} = 2 \times 10^{-8} hd + 9.96 \times 10^{-5} \rho^2, \tag{2.10}$$

where d and ρ are in microns and h is in electron volts. Therefore, for hard spheres the van der Waals force is proportional to the particle size (micro-particle sizes are commonly referenced in terms of diameters of the particle).

2.1.3 Electrostatic Forces

The electrostatic forces that bind a particle to a surface are probably the forces one is most familiar with. This is mainly due to the dominance of this binding force for large particles. In discussing electrostatic forces there are two types of this force to consider. The first is due to an excess bulk charge on either the particle or the substrate which results in an electrostatic force between the pair. The initial bulk charge may induce an opposite local charge in the adjacent material which leads to an attractive force. This electrostatic force is called the *image force* and the situation

with initial particle charge is depicted in Figure 2.2. The image force (F_i) can be expressed as

$$F_i = \frac{q^2}{4\pi E e l^2}, \tag{2.11}$$

where q is the charge, E is the permittivity of free space, e is the dielectric constant of the medium between the particle and substrate and l is the distance between charge centers. The charge on a particle can be expressed as

$$q = CU = 4\pi E a U, \tag{2.12}$$

where C is the capacitance and U is the potential. Therefore, the image force that results from a charged particle is

$$F_i = \frac{4\pi E a^2 U^2}{e l^2}. \tag{2.13}$$

For this case of net particle charge, Equation (2.13) can be further reduced to an approximate expression involving just the particle diameter. According to Bowling, the capacitance of the particle can be approximated to be a function of the particle radius and the charge center distance is approximately twice this radius. This leads to the approximate expression

$$F_i = 3 \times 10^{-10} d^2, \tag{2.14}$$

where d is the particle diameter in microns. Equation (2.14) assumes a charge density of 10 elementary charges per square micron (Bowling comments that this might be considered a large charge density).

Even in the case that either the particle or substrate is not initially charged there can still be an electrostatic binding force. This is due to a contact potential that develops between two different materials when in contact. The difference in the materials work functions and local energy states results in an electron transfer between

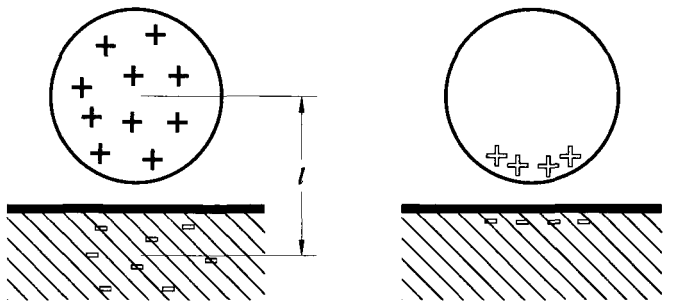

Figure 2.2: The two possible electrostatic forces that may bind a particle to a surface. The image force is due to excess bulk charges on either the particle or substrate. The double layer force results from a contact potential due to electrical properties of both sphere and substrate materials. In the figures, solids correspond to permanent charges while outlines refer to temporary or induced charges.

the materials which, when the current flow between the materials is in equilibrium, creates an electric double layer. This results in an electrostatic force between the particle and substrate and it is commonly called the electrostatic *double layer force* (F_{el}). This situation is depicted in Figure 2.2 and the magnitude of the force is given as

$$F_{el} = \frac{\pi E a U^2}{z} \quad \text{dynes}, \tag{2.15}$$

where U is the contact potential between the particle and substrate and z is the separation distance between the particle and substrate surfaces in microns. This can approximately be reduced to (z is again assumed to be 4 Angstroms)

$$F_{el} = 4 \times 10^{-8} U^2 d, \tag{2.16}$$

where d is in microns. According to Bowling, the value of the contact potential generally ranges from 0.0 to 0.5 volts.

Equations (2.14) and (2.16) are approximate expressions that should give an idea of the strength of the electrostatic binding forces. However, this discussion has not specifically taken into account the nature of the charges in different materials.

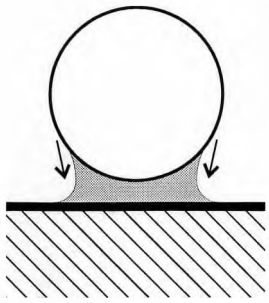

Figure 2.3: The capillary force results from a layer of liquid between the sphere and the substrate. The surface tension of the liquid binds the particle to the surface.

Bowling mentions that for conductors the electrostatic attraction is quite small. Since electrons are mobile in the material, only surface charge layers will exist and any excess charge is balanced by contact charge flow. However, for good insulators the situation is reversed. The inability of electrons to flow in the material results in relatively large charge regions (compared to the surface layers of conductors) and significant electrostatic forces. The size dependence of the two electrostatic forces vary; the image force is linearly proportional to the size whereas the double layer force is proportional to the square of the particle size. This implies that for the larger particles the double layer force will be the stronger electrostatic force and for a the smaller particles the image charge is stronger (see Figure 2.4).

2.1.4 Capillary Force

If there exists some liquid on the substrate surface it can lead to another binding force. The strength of this force depends on the amount of liquid present. If there is a sufficient amount of liquid to immerse the particle the result is that the van der Waals force is reduced. However, if there only exists a relatively small amount of liquid between the surface and the particle, the surface tension of the liquid tends to hold the sphere onto the surface. This situation is depicted in Figure 2.3 and this

binding force is generally termed the capillary force. The magnitude of this force is given as

$$F_{cap} = 4\pi a\gamma \quad \text{dynes}, \tag{2.17}$$

where γ is the liquid surface tension. In newtons the expression for the capillary force becomes

$$F_{cap} = 6.3 \times 10^{-6}\gamma d, \tag{2.18}$$

where d is given in microns and γ is in N m^{-1}. A key point in this case is that if the particle and liquid are not mutually attractive the capillary force will be zero. For example, if the particle is hydrophobic and the liquid is water, the water will not adhere to the particle. The absence of the water's surface tension results in a null capillary force. If there is attraction, the force does vary linearly with the particle size.

2.1.5 Comparison of Binding Forces

The expressions for the several types of binding forces are not all exact. Some equations are based on approximations which, in the current case, are reasonable. The values used in the calculations are not exact either. They are representative of the types of materials used in the experiments, but are not exact numbers for the specific materials of the micro-particles or substrate. However, the equations will, to a first approximation, outline the relative strengths of the forces. As well, the equations do show the relationship between the binding force and the size of the particle.

Table 2.1 lists the magnitude of the binding forces on a 2 μm polystyrene (PS) micro-sphere on a silicon substrate in order of decreasing strength (the size of micro- and nano-particles is commonly referred to in terms of the particle diameter). The capillary force was calculated for water with a surface tension of 73 mN m^{-1} at

Binding Force	Force (nN)
Capillary	920
van der Waals (2% deformation)	180
van der Waals (undeformed)	92
Electrostatic Double Layer	20
Electrostatic Image	1.2
Gravity	4.6×10^{-5}

Table 2.1: Comparison of the binding forces acting on a polystyrene (PS) micro-sphere with a diameter of 2 μm on a silicon substrate. PS physical data taken from reference [17] and Si data taken from reference [18].

25 °C. If water is present under the sphere it certainly is the dominant binding force. However, without any moisture, the van der Waals force does play the most significant role examined in binding. This force was calculated by combining the Lifshitz–van der Waals constants for a silicon micro-sphere on a silicon substrate (6.8–7.2 eV) and for a polymer micro-sphere on a polymer substrate (0.6–0.9 eV). Taking the average of these values and using the approximation [13]

$$h_{poly-Si} \approx \sqrt{h_{poly-poly} h_{Si-Si}}, \tag{2.19}$$

the value of 2.29 eV was determined. For the effect of deformation Equations (2.9) and (2.10) were used. As can be seen, the effect of deformation can be quite significant with a doubling of the undeformed van der Waals force. At this radius, Table 2.1 also shows that electrostatic forces are relatively insignificant. The role of gravity on these micro-particles can be neglected as is also seen from the table.

Since the forces' proportionality with the particle size varies, the calculations have also been performed over an applicable size range. Figure 2.4 shows the magnitudes of the binding forces over a particle size range from 100 nm to 100 μm. It shows that the van der Waals forces are certainly the strongest given that conditions are dry. The enhancement of the van der Waals force due to particle deformation

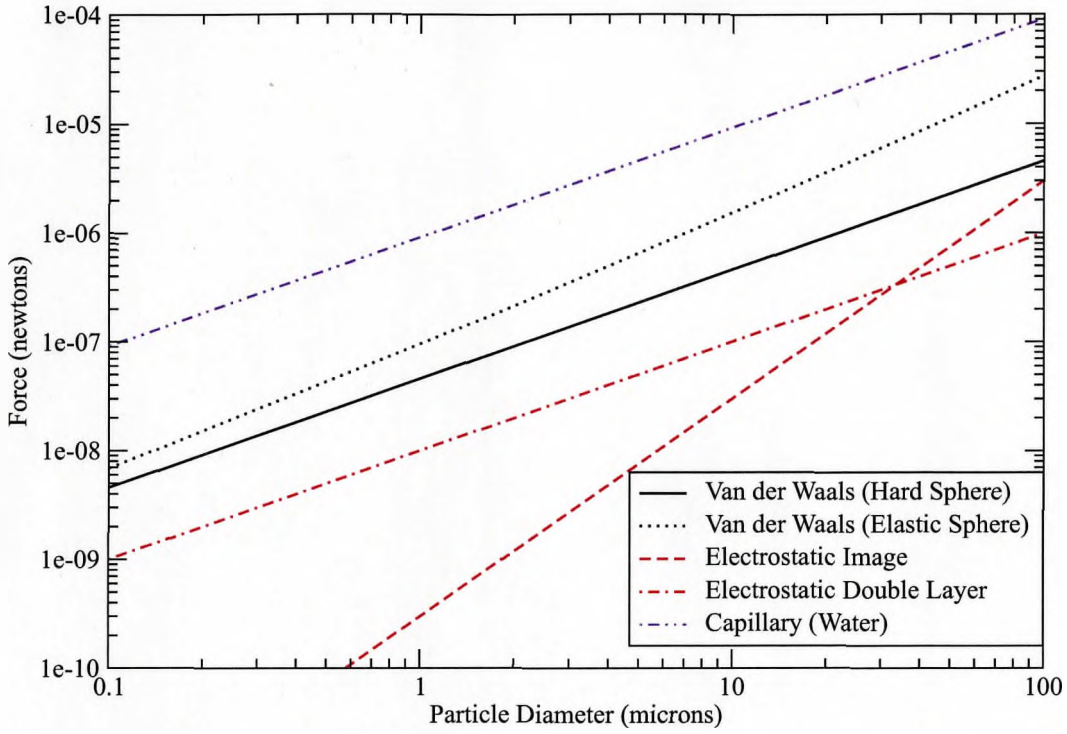

Figure 2.4: Dependence of the particle size on binding forces. The calculations were performed for a PS micro-sphere on a Si substrate with the same data and methods used for Table 2.1.

also increases with size. Figure 2.4 also shows that for particles in the size range of the current work (around 2 μm), the electrostatic forces are insignificant compared to the van der Waals force. It therefore appears that under dry conditions where there is no liquid on the substrate, the main binding force would be the van der Waals force provided that other binding forces not considered (such as chemical bonding) are insignificant.

2.2 Removal Mechanisms

From the previous section it becomes obvious that removing micro-particles from surfaces is not achieved by simply turning the surface upside down to let gravity do all the work. In some manner a strong force must be produced to overcome the strong

binding forces. One such way to produce these strong forces is through surface irradiation by nanosecond, picosecond and femtosecond pulses of light which has resulted in the removal of the micro-particles from the surfaces. At first it was speculated by us that forces due to the intensity gradient of the pulses could be responsible for this removal. With closer and more careful examination of the problem, other methods presented themselves as being better possibilities. This section will consider some possible mechanisms behind the removal of the micro-particles from the substrate surface. As well, a brief discussion of their magnitudes will be presented. The following list is not exhaustive; there may exist other methods which may be employed to remove the micro-particles. One such example is the use of a repetitive pulse irradiation at a frequency which is resonant with micro-particle deformations. This is analogous to hitting a basketball lying on a floor with the right force at the right rate. If this is done correctly, one can eventually dribble the ball and it has been effectively removed from the floor. As well, the mechanisms are presented in a manner which pertains to micro-particle removal, yet they may also be of interest to other micro-manipulation studies.

2.2.1 Light Forces

It is well known that photons carry momentum and that there is a momentum pressure on objects irradiated by light. For macroscopic objects illuminated by conventional, low-intensity light sources this radiation force is negligible due to the large inertia of the object. However, for smaller objects and high intensity lasers, this force can be large enough to manipulate the object. It may strong enough to overcome micro-particle binding to substrates and, therefore, prove to be a force responsible for the removal of the micro-particles.

Light forces can be divided into two spatial components: the scattering force

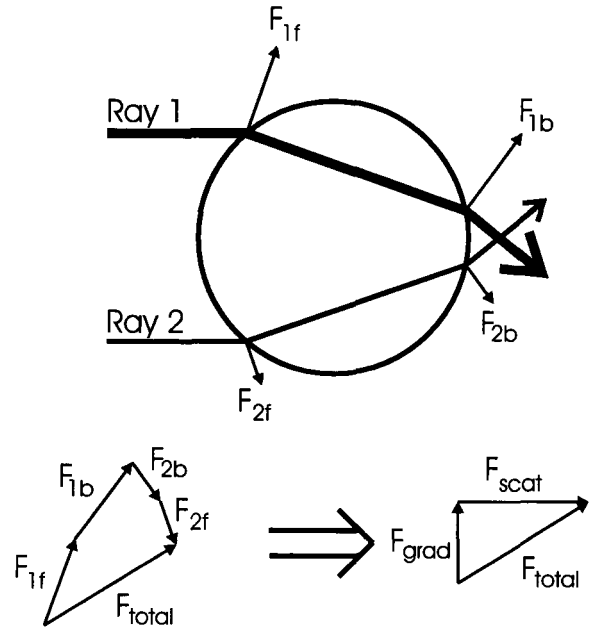

Figure 2.5: The light forces acting on a particle in the ray-optics regime. The top of the figure shows the total force at each interface (F_{1f}, F_{2f}, F_{1b}, and F_{2b}) and on the bottom the vector sums of these forces is shown (left vector diagram). The sum of these forces results in a total force (F_{total}) acting on the sphere (when only considering two rays) which is subsequently divided into the orthogonal components of the scattering and gradient force (F_{scat} and F_{grad} in the right vector diagram, respectively).

and the gradient force. The scattering force is the component that is associated with the radiation pressure; it is the component that is directed along the direction of light propagation. The gradient force can be either perpendicular or parallel to this direction and it specifically results from intensity gradients along the beam of light. Figure 2.5 is a representation of the light forces acting on a sphere in the ray-optics regime where the size of the sphere is much larger than the wavelength. In this regime, the light force can be determined from momentum transfer of the photons at the material boundaries. The top part of Figure 2.5 depicts the total force at the front (subscript f) and back (subscript b) interfaces for two rays. Each of these forces is a sum of the momentum transfer to the sphere due to both reflection and

refraction. Therefore, F_{1f} is the net force from ray 1 (subscript 1) at the front interface due to reflection and refraction of this ray at this particular material interface. This formalism provides an intuitive view of the origin of the light force.

In order to determine the total light force acting on a sphere, all rays traveling through the sphere have to be integrated over. Figure 2.5 also shows two rays which are located an equal distance from the center of the sphere. This will illustrate the nature of the light forces without having to deal with any integration over many rays. The incident beam profile of light is taken to be Gaussian and is collimated with the maximum intensity being located slightly above the sphere's center. This results in the intensity of Ray 1 being greater than Ray 2. The figure also shows the total force acting at each interface and is dependent on the intensity of the ray. Since a ray with a greater intensity has more photons carrying momentum passing through the sphere in a given time, the momentum transfer to the sphere is greater and thus, the light force will be greater. The bottom of Figure 2.5 shows the total force (F_{total}) that results from the two rays. It has been divided into the two components: the scattering force (F_{scat}) and the gradient force (F_{grad}). The scattering force is taken to be along the beam axis and therefore the gradient force is perpendicular to the beam and it is directed toward the maximum intensity. If the beam intensity distribution were aligned with the sphere, there would be no gradient force since the intensities in ray 1 and 2 would be the same. This same argument will also work for a focussed beam. In this case, a gradient force would also exist along the axis of the laser beam due to the axial intensity distribution.

While the ray approach gives an intuitive description of the nature of light forces, it is not applicable to the situation of the present material. The particle sizes used in this work are of the same order of magnitude as the wavelength and,

therefore, the nature of the light is not adequately described by the ray picture. In order to determine gradient forces Tlusty *et al.* have proposed a method of calculation for a focussed Gaussian beam which is accurate for all particle sizes [19]. The method involves the use of the beam's energy density ($\mathcal{E}$) which is taken in cylindrical coordinates as

$$\mathcal{E}(\rho, z) = \mathcal{E}_o \exp\left(-\frac{\rho^2}{2\omega^2} - \frac{z^2}{2\omega^2\varepsilon^2}\right), \tag{2.20}$$

where $\mathcal{E}_o$ is the energy density at the focus, ε is the eccentricity of the beam, ω and $\omega\varepsilon$ are the transverse and axial beam waists respectively, and (ρ, z) are the cylindrical coordinates. In the case that the eccentricity is unity, the gradient force can be given, with $a \ll \omega$, in spherical coordinates as

$$F_{grad}(r) = \frac{4\pi}{3}\alpha\mathcal{E}_o\omega^2\beta^3 u e^{-\frac{u^2}{2}}, \tag{2.21}$$

where

$$\alpha = n^2 - 1, \quad \beta = \frac{a}{\omega}, \quad \text{and} \quad u = \frac{r}{\omega}, \tag{2.22}$$

where n is the index of refraction of the sphere and r is the radial spherical coordinate. However, in practice the eccentricity of the focussed beam is not unity and in this case the gradient force can be approximated with reasonable accuracy by

$$F^{\rho}_{grad}(\rho) = \alpha\mathcal{E}_o\omega^2 A_\rho(\varepsilon) e^{-\frac{u_\rho^2}{2}} \sinh(a_c u_\rho), \tag{2.23}$$

$$F^{z}_{grad}(z) = \alpha\mathcal{E}_o\omega^2 A_z(\varepsilon) e^{-\frac{u_z^2}{2}} \sinh(a_c u_z), \tag{2.24}$$

where $u_\rho = \rho/\omega$, $u_z = z/\omega$, and

$$A_\rho(\varepsilon) = 4\pi\varepsilon \operatorname{erf}\left(\frac{a_c}{\sqrt{2}}\right) \operatorname{erf}\left(\frac{a_c}{\sqrt{2}\varepsilon}\right) e^{-\frac{a_c^2}{2}}, \tag{2.25}$$

$$A_z(\varepsilon) = 4\pi \operatorname{erf}\left(\frac{a_c}{\sqrt{2}}\right)^2 e^{-\frac{a_c^2}{2\varepsilon^2}}, \tag{2.26}$$

$$a_c = \frac{a}{\omega}\left(\frac{\pi}{6}\right)^{1/3}. \tag{2.27}$$

Examples of the magnitude and nature of the gradient force are shown in Figure 2.6 for both the axial and radial directions. The figure shows that the gradient force acts to push the particle into the focal spot of the beam. As well, if the particle is located too far from the focal spot, the gradient force will not affect the particle. However, there is still the scattering force and Tlusty *et al.* mention that it is approximately given by

$$F_{scat} \sim \alpha^2 \mathcal{E}_o \lambda^2 \left(\frac{a}{\lambda}\right)^6 \quad \text{for } a \ll \lambda, \tag{2.28}$$

$$F_{scat} \sim \alpha \mathcal{E}_o \omega^2 \quad \text{for } a \gg \lambda, \tag{2.29}$$

and acts in the direction of the light propagation. The light force equations also indirectly show that, for light pulses, a shorter pulse length will result in a larger force provided that the pulse fluence (or pulse energy) stays the same. This can be seen in the expression of the energy density for a light pulse (under the simplification of a "top hat" intensity profile)

$$\mathcal{E}_o = \frac{I}{c} = \frac{\mathcal{F}}{c\tau_p}, \tag{2.30}$$

where I is the pulse intensity, $\mathcal{F}$ is the pulse fluence and τ_p is the pulse length. Equation (2.30) shows that a decrease in the pulse length results in an increase in the energy density and, therefore, an increase in the light force with all other parameters the same.

The light forces may also turn out to be significantly different in the case of high light intensity. This is due to the optical non-linearity of the medium. Pobre *et al.* performed numerical calculations on the light force considering the electro-optic Kerr effect [20] and showed that the Kerr effect can significantly alter the light force. For a micro-sphere with a diameter of 17 μm and Kerr coefficient of 10^{-5} m^2 W^{-1}, the effects start to appear around pulse peak powers of 1 MW (this would correspond

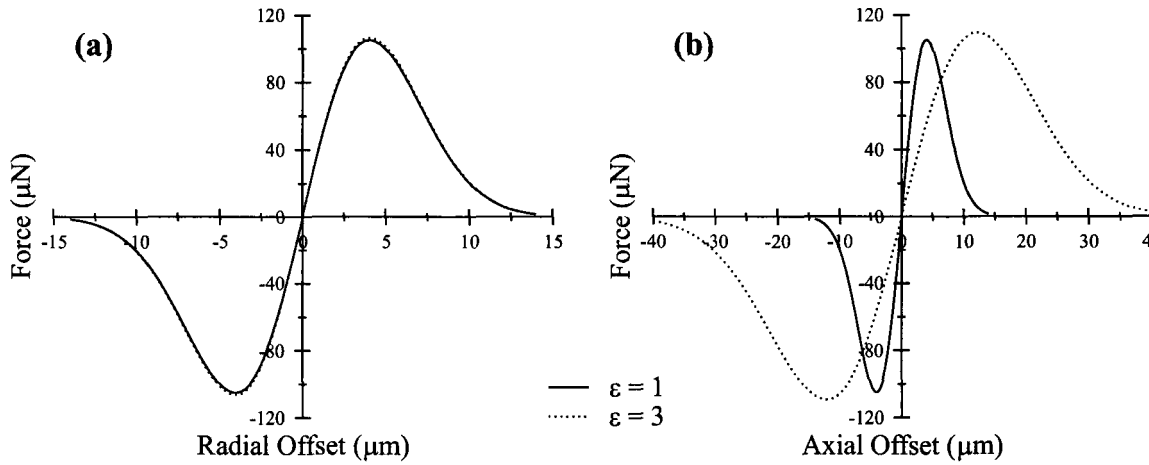

Figure 2.6: Calculations of the gradient forces acting on a micro-sphere in the (a) radial and (b) axial directions. The calculations were performed with $\lambda = 800$ nm, $a = 1.5$ μm, $\omega = 4$ μm, $\mathcal{F} = 50$ mJ cm^{-2}, $n_{int} = 1.6$, $n_{ext} = 1.0$ and $\tau_p = 100$ fs.

to a 100 fs pulse with an energy of 100 nJ). The non-linearity acts in a way which counteracts the linear light force; initially the total force is decreased but at a higher pulse power (in their calculations it was only several MW), the direction of the total force is reversed and the magnitude of the force increases with increasing pulse power. This results in large light forces, but any trapping ability of the force is lost. The pulse energies at which non-linearity can be observed is quite high for the present work. Therefore, it is not likely that non-linearity of the materials used would lead to a significant interaction and removal of the micro-particles.

When evaluating the means in which the light force could act as a removal mechanism there are several possibilities to consider. First of all, if the focus of the beam is at the sphere center, there will be no gradient force. In fact, Figure 2.6 shows that the maximum forces on the particle are experienced at the beam waist (ω and $\omega\varepsilon$ for the radial and axial directions, respectively). In regards to the method in which the micro-particle removal takes place, the location of the particle in the beam would be of vital importance. The axial gradient force can act to either push

the particle into the surface or pull it off. If the particle is pulled off the surface, the gradient force is itself responsible for the removal whereas if the particle was pushed, the particle may be deformed by the gradient force. In this case it may be possible that the elastic relaxation of the particle is sufficient to remove it from the surface. The scattering force must also be considered since it is roughly of the same order of magnitude as the gradient force. It always acts into the surface and may then either increase or decrease the total axial force acting on the particle. In terms of the radial gradient force, if the beam is not incident perpendicular to the surface and the focus is above the particle, it may be possible that the particle is removed.

2.2.2 Ionization and Electrostatic Forces

Another possible removal mechanism could be due to electrostatic forces. Just as they can act as a binding force, through ionization of the particle and substrate, they can also act to remove the particles. The quantitative description of this mechanism is not a trivial undertaking and, for the scope of this work, the arguments will only be given in qualitative form. While the photon energy is most likely not large enough to ionize the materials directly, the intensity of the focussed beam is typically on the order of 10^{11}–10^{13} W cm^{-2} and may lead to multi-photon ionization. The positive charge of the substrate and particle could then result in an electrostatic force that is strong enough to remove the particle. To a first approximation, the strength of this force would depend on two parameters: the rate of ionization and the initial charges of the substrate and particle. These parameters likely depend strongly on the materials used, but in the current work it is not believed that ionization plays a significant role in the removal of micro-particles.

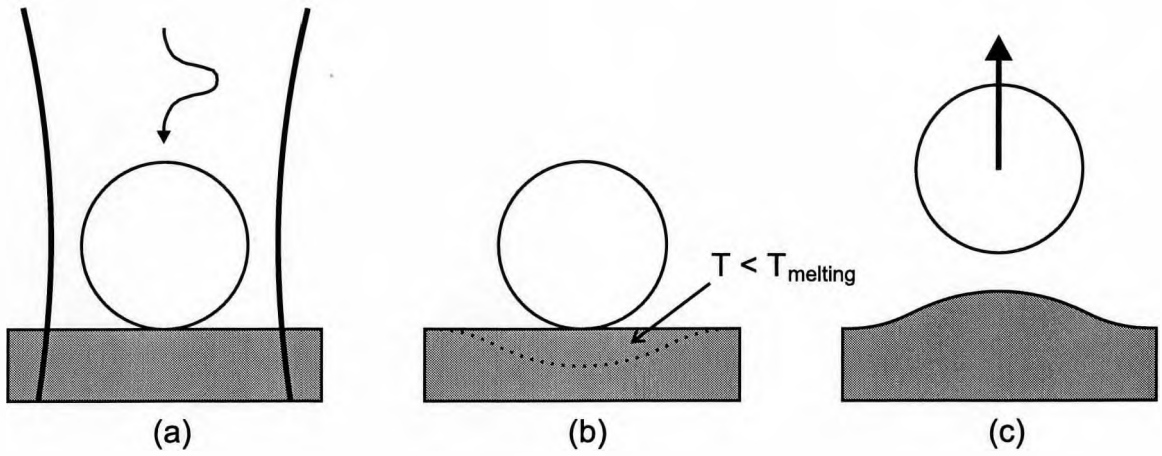

Figure 2.7: Mechanism of micro-particle removal through material expansion of the substrate: (a) The particle and substrate are irradiated with the short laser pulse. (b) The substrate absorbs the pulse energy resulting in a temperature rise in the irradiated area. The temperature of the substrate is below its melting point. (c) The substrate expands providing the micro-particle with a large enough force to overcome binding forces as well as sufficient energy for complete removal. The substrate and particle are undamaged.

2.2.3 Material Expansion

While the previous removal mechanisms may be possible, and could prove to be interesting for a wide variety of applications, it is commonly accepted that, with the use of nanosecond pulses in removing micro-particles, the expansion of either the particle or the substrate is responsible for micro-particle removal from the surface [8,21–29]. In the literature this model is commonly called the Thermo-Elastic model. An initial question that was asked when the current work was in its early phases was whether the same process would be responsible for micro-particle removal with femtosecond pulses of light.

The idea behind this mechanism is shown in Figure 2.7. The incident light pulse will be partially absorbed (or totally absorbed depending on the materials) by either the particle, the substrate or both. This absorbed energy results in a

local temperature rise which is assumed to be below the melting temperature of the material. As a result of the increased temperature, the material expands exerting a force on the particle which is great enough to overcome the binding force. It is also possible, if the particle or substrate material is elastic enough, that there will be deformation of the materials and through their subsequent expansion an additional force due to deformation could help facilitate particle removal.

The amount the substrate surface expands in a given amount of time t can be given as

$$L_s(t) = \int_o^L \gamma \Delta T(z,t) dz, \tag{2.31}$$

where L is the substrate thickness, γ is the linear thermal expansion coefficient, z is the direction perpendicular to the surface. As well, $\Delta T(z,t)$ is the temperature change given by

$$\Delta T(z,t) = T(z,t) - T_o, \tag{2.32}$$

where $T(z,t)$ is the temperature at time t and distance z below the surface and T_o is the initial temperature of the substrate. The temperature of the substrate at time t and position z can be determined through the equation

$$\rho_s(T) c_p(T) \frac{\partial T(z,t)}{\partial t} = \frac{\partial}{\partial z}\left[K(T)\frac{\partial T(z,t)}{\partial z}\right] + (1 - R_s)\alpha I_o e^{-\alpha z}, \tag{2.33}$$

where $\rho_s(T)$ is the density, $c_p(T)$ the specific heat, $K(T)$ the thermal conductivity of the substrate at temperature T and R_s, α and I_o are the surface reflectivity, the absorption coefficient and the intensity of the incident beam, respectively [8]. Given the temperature profile of the parameters, Equations (2.31) and (2.33) would have to be solved numerically. However, Vereeke *et al.* [29] have presented approximate

expressions for the surface temperature change and expansion of the surface as

$$\Delta T = 2.26F\frac{1-R_s}{c_p\rho_s\delta_p}, \tag{2.34}$$

$$L_s^{max} = \gamma\delta_p\Delta T, \tag{2.35}$$

where F is the pulse fluence and δ_p is the heat diffusion length during the pulse. Using these approximations, an order of magnitude estimation of the surface acceleration is

$$a = \frac{L_s^{max}}{\tau^2}, \tag{2.36}$$

where τ is the period of time in which the substrate expands. The particle should experience the same acceleration as the substrate surface and the force on the particle is thus

$$F_{me} = \frac{mL_s^{max}}{\tau^2}, \tag{2.37}$$

where m is the mass of the particle. A key parameter in the above equations is τ. In the nanosecond work, this time is believed to be on the order of the pulse length. However, for a femtosecond pulse the response of the substrate will not coincide with the duration of irradiation. This is due to the nature of energy absorption and heat transfer in the material; energy is initially absorbed by the electrons and then transferred to the lattice on a time scale of approximately 1–10 ps [30]. For a femtosecond pulse it is only the electrons that carry the excess energy on the timescale of the irradiation and, therefore, no expansion occurs. However, over a longer period of time, which may be less than several nanoseconds, energy is transferred to the lattice and the expansion of the surface is realized—provided a different removal mechanism does not remove the particle before this occurs.

Lu *et al.* [8] have also investigated the additional effect of the deformation of the particle and its elastic restoring force. They give the elastic repelling force as

$$F_e = \frac{4E\sqrt{R}}{3(1-\sigma^2)}L_p(t)^{\frac{3}{2}}, \tag{2.38}$$

where L_p is the deformation with respect to time (this is the same as the deformation parameter δ in Figure 2.1). The potential energy of the deformation is given as

$$W_e = \frac{8E\sqrt{R}}{15(1-\sigma^2)} L_p(t)^{\frac{5}{2}}. \tag{2.39}$$

The calculation of the time variation of the deformation is not a trivial undertaking but Equations (2.38) and (2.39) can be used to calculate the initial deformation. The contribution to the total cleaning force can then be approximated by assuming all of the energy of the deformation goes into the removal.

2.2.4 Material Ablation

In the previous section the possibility of absorption of light energy leading to the expansion of the substrate was discussed. It was assumed that the temperature of the substrate would stay well below its melting temperature. It is possible that the energy absorbed by the material could lead to a larger temperature rise and melting could occur. For a femtosecond pulse ablation could occur when the energy absorbed is too great in too short of a time. In this case, the material cannot dissipate the energy and an "explosive melting" occurs.

The basic idea of this mechanism is shown in Figure 2.8. It should be noted that the material can either ablate off the substrate or the particle. In either case, the ablated material carries momentum and kinetic energy. It is through conservation of momentum and energy that the removal mechanism is facilitated. If the material comes from the particle there is a recoil of the particle, and if the material comes from the substrate surface it will transfer momentum to the particle by contact. The effectiveness of this mechanism in removing particles from the surface relies on two main parameters: the amount and velocity of the ablated material. Cavalleri *el al.* have performed time of flight mass spectroscopy with femtosecond ablation of gallium

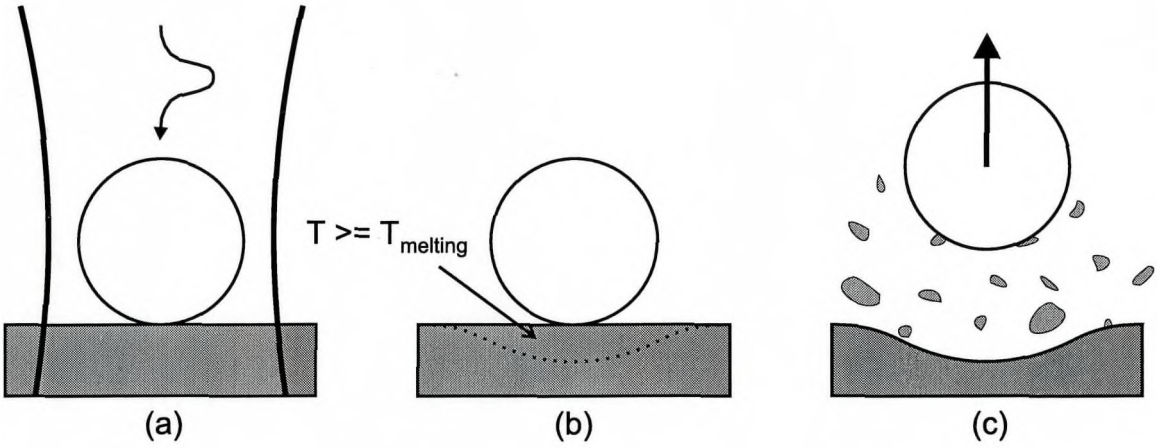

Figure 2.8: Mechanism of micro-particle removal through ablation of the substrate: (a) The particle and substrate are irradiated with the short laser pulse. (b) The substrate absorbs the pulse energy resulting in a temperature rise in the irradiated area. The temperature of the substrate is near or above its melting point. (c) Material is ablated off the surface which provides momentum and energy to the micro-sphere. The micro-sphere is ejected from the surface but the substrate is permanently damaged.

arsenide and found an average ablated gas center-of-mass drift velocity to be 528 m s^{-1} [31]. The velocity of the ablated gas is probably different for differing materials, yet this value would represent the order of magnitude of the gas velocity for most materials. The other unknown quantity is the amount of material ablated. Cavalleri *et al.* have also studied the amount of material ejected around the ablation threshold for gallium arsenide and silicon. Their results show that the amount of material removed from the surface increases with increasing pulse fluence. But perhaps the more interesting result is that there is material removed from the surface even below the ablation threshold. In some cases, the amount of the removed material may not significantly change over a reduction of the fluence by a half. Therefore, ablation may not only a possible removal mechanism for fluences above ablation thresholds, removed material below ablation thresholds may also result in micro-particle removal from surfaces.

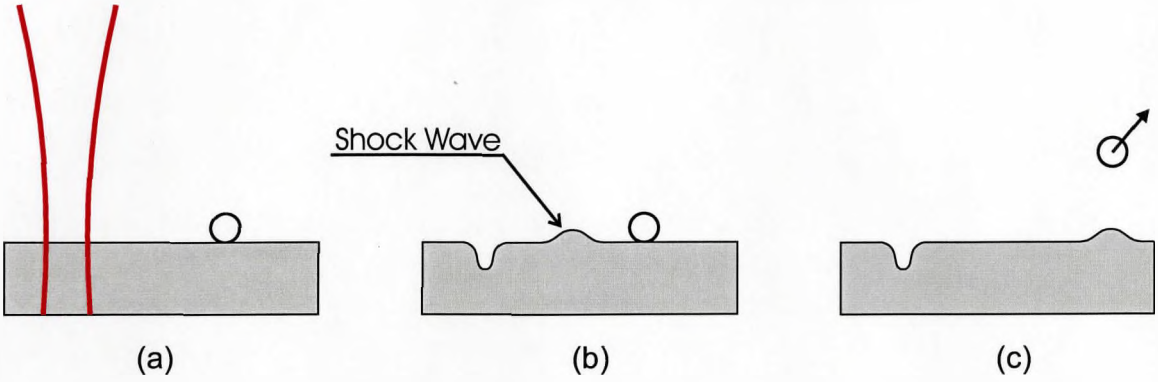

Figure 2.9: Example of a method in which a shock wave produced by substrate irradiation can result in removal of micro-particles: (a) The substrate is irradiated with the laser pulse. (b) Ablation results in a shock wave that travels through the medium and in the air (which is not shown). (c) The shock wave traveling near the surface can result in the removal of the particle.

2.2.5 Shock Waves

There is another possible method which could result in micro-particle removal and is closely tied with material ablation and expansion. This is through shock waves which would be created near the ablation threshold and they are depicted in Figure 2.9. D.S. Moore *et al.* have irradiated a 1 μm thick aluminium film which was deposited on a glass substrate with 120–400 fs pulses at a wavelength of 800 nm [32,33]. The experiment was carried out such that they measured the amplitude (the displacement of the aluminum–air surface) of the shock wave on the opposite side of the irradiated aluminum sample. After the wave had traveled through 1 μm of aluminum the displacement was roughly 8 nm for a pulse fluence near the ablation threshold. No comments on the wave velocity or wave-crest width were made but J Lee *et al.* have measured shock wave velocities in a glass micro-sphere [34]. Using a Q-switched Nd:YAG laser (wavelength: 1.06 μm; pulse length: 10 ns) at a fluence of approximately 3 mJ cm^{-2} the shock wave velocity was between 2–3.5 km/s (this depended on the angular position where the measurement occurred) and appeared

to increase linearly to around 6–9 km/s at an approximate fluence of 10 mJ cm^{-2}. The forces produced by the shock waves are not exactly known but they are able to remove micro-particles. Lee *et al.* have devised a method of dry laser cleaning based on shock waves [35]. This involved ionizing the air directly above a silicon surface which contained titanium micro-particles and resulted in shock waves which effectively removed the micro-particles. They also irradiated the surface using a pulse with a fluence significantly greater than the ablation threshold, which resulted in an ablation crater with a diameter of 2 mm and a cleaned area of about 2.5 cm^2. Therefore, in certain situations, another thermal type of mechanism can be responsible for micro-particle removal: material shock waves.

2.2.6 Comparison of Removal Mechanisms

Several possible removal mechanisms have been presented but the probability of any of them being responsible for removal has not been discussed. While the mechanism that is responsible for removal has to be determined through experimentation, the current discussion should present a rough outline of certain mechanisms' validity. The results of some first-order estimates of the removal forces and particle kinetic energies are given in Table 2.2. The calculations were performed for a PS micro-sphere with a diameter of 2 μm on a silicon substrate. The particle energy for the ablation mechanism was determined by assuming a cylindrical volume with a diameter of 400 nm and depth of 50 nm to have been removed from the substrate. The total momentum of the ablated material was determined using a center-of-mass velocity of 500 m s^{-1}. The velocity of the ejected particle—and subsequently, its kinetic energy—was determined by assuming 75% of the ablated material's momentum is transferred to the micro-particle. The force acting on the particle is then crudely determined

Removal Mechanism	Force (μN)	Energy (eV)
Ablation	5.5×10^{3}	2.0×10^{4}
Expansion (1 ns)	1.2	980
Expansion (10 ns)	1.2×10^{-2}	9.8
Light Force	3.9	2.0×10^{-4}

Table 2.2: Comparison of several removal mechanisms for a polystyrene micro-sphere from a silicon substrate. The parameters used in the calculation are $n = 1.6$, $a = 1$ μm, $\tau_p = 140$ fs, $\omega = 4.7$ μm and $\mathcal{F} = 10$ mJ cm^{-2} (corresponding to an approximate pulse energy of 7 nJ). Thermophysical data taken from [17,18].

from

$$KE_o = \frac{F^2\tau^2}{2m}. \tag{2.40}$$

where τ is duration during which the force acts on the particle. For the ablation calculation this time was taken to be 1 ps. For the expansion model the force is determined from Equation (2.37) and the initial kinetic energy of the particle is then determined from Equation (2.40) using τ values of 1 ns and 10 ns. The light force is determined from Equation (2.21) with a fluence of 10 mJ cm^{-2} and the micro-particle location was set at the beam waist. Again, the kinetic energy is determined from Equation (2.40) where τ in this case was 140 fs representing the pulse length.

A quick examination of Table 2.2 shows that the calculated removal mechanisms all provide forces greater than the binding forces. The strongest of these forces is through ablation of material. This mechanism could produce around 5.5 mN of force, but this strongly strongly depends on the duration of ablation which is not known exactly. If the ablation time were increased to 1 ns, the force would be on the order of 10^{-6} Newton but the energy would stay the same. As long as the force produced is stronger than the binding force this mechanism would be the most effective in removing micro-particles large distances from the surface. The material expansion mechanism could be the second strongest mechanism. The forces produced are not

as large as by ablation, but for a reasonably short pulse they are larger than the binding forces. However, the 10 ns expansion would not likely result in removal since the corresponding force is smaller than the calculated van der Waals force for a 2 μm PS micro-sphere (see Table 2.1). As the time of the expansion decreases, the force and energy of the particle do increase. The final force examined was the light force and it does provide a force that is greater in magnitude than the material expansion mechanism. However, due to the very short duration of the pulse, the energy imparted to the particle is very small and would, in this case, only result in a vertical displacement of about 3 nm. This certainly is not significant enough to remove the particle from the surface.

In this section there are two removal mechanisms where order of magnitude estimates of their strength cannot be made. One is ionization and the resulting electrostatic force. The discussion of the validity of this mechanism behind the removal of micro-particles will have to be left to experimental results. The other unevaluated removal mechanism is due to shock waves. The forces produced by such waves would be strong enough to remove the micro-particles as was seen by Lee *et al.* [35]. If this mechanism were to be responsible for removal, it would also be expected that any particle located close to the targeted one will also be removed. This can certainly be determined through experimentation. In terms of the other mechanisms already discussed in this section, the light force would not be responsible for removal. This leaves either material expansion or ablation, both of which could be strong enough to remove the micro-particles.

Chapter 3

Mie Theory Calculations

In the discussion of the theoretical details behind the interaction of light pulses with micro-particles, an important consideration is the local or near field distribution of light around the particle. The nature of this electromagnetic field depends strongly on the wavelength of light, the particle size and the index of refraction of the materials. It may have a significant effect on the actual interaction that is responsible for removal of the micro-particles from the substrate surface. In order to understand these fields, some calculations were performed of the electromagnetic field surrounding micro-spheres using Mie theory. This treatment was not done rigorously since the substrate surface was not included in the calculation. As well, only monochromatic light and linear material properties were considered. Despite this the calculations should give a reasonable estimate of the field intensities and indicate the physical properties of the electromagnetic fields and their dependence on the parameters involved.

In this chapter the theoretical basis of Mie theory and the numerical techniques employed in the calculations will be discussed. Several results of the electromagnetic field calculations will also be presented and the validity of these results will be discussed.

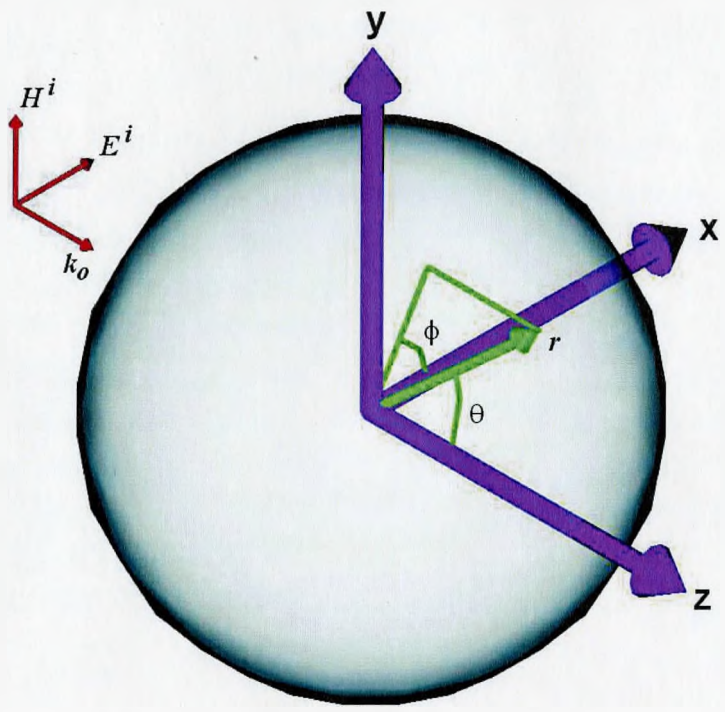

Figure 3.1: Summary of the geometry used in the Mie theory calculations. The plane-wave travels in the positive z direction with a polarization along the x-axis.

3.1 Mie Theory

The optical properties of metallic particles have been studied by various scientists, but it was not until 1908 that G. Mie [36] developed a rigorous theory of diffraction for these particles. His theory applies to any size of a homogeneous sphere surrounded by a homogeneous, non-conducting medium and an incident plane-wave. The following is a summary of the theory that Mie developed according to the presentation of Born and Wolf [37].

In the following derivation of the electromagnetic field around spheres both mediums are assumed to be non-magnetic and isotropic. The incident light is taken to be a linearly polarized plane-wave. The time dependence of the fields is $exp(-\imath\omega t)$ and the spherical coordinate system is used. The physical situation is shown in Figure

3.1 where the superscript I refers to the medium outside the sphere and II to the medium inside the sphere. The electromagnetic fields satisfy Maxwell's equations and the derivation begins with

$$\begin{aligned} \vec{\nabla} \times \vec{H} &= -\tilde{k}_1 \vec{E}, \\ \vec{\nabla} \times \vec{E} &= k_2 \vec{H}, \end{aligned} \tag{3.1}$$

where

$$\tilde{k}_1 = \frac{\imath\omega}{c}\left(\epsilon + \imath\frac{4\pi\sigma}{\omega}\right) = \frac{\imath\omega}{c}\tilde{n}^2, \tag{3.2}$$

$$k_2 = \frac{\imath\omega}{c}, \tag{3.3}$$

with ω the frequency of light, c the speed of light in vacuum, $\tilde{n}$ the complex index of refraction (tildes will represent complex scalars), and ϵ and σ the dielectric constant and conductivity of the medium, respectively. The wave vector of the light ($\tilde{k}$) is given by

$$\tilde{k} = \sqrt{-\tilde{k}_1 k_2} = \frac{\omega\tilde{n}}{c}, \tag{3.4}$$

where the wave vector outside the sphere is real and inside it is complex (due to the index of refraction). If the incident wave is normalized to unity (i.e. $|\vec{E}^i| = 1$) and the polarization is along the x-axis, the incident electromagnetic field becomes

$$\begin{aligned} \vec{E}^i &= e^{\imath k^{(I)} z}\hat{e}_x, \\ \vec{H}^i &= \tfrac{\imath k^{(I)}}{\tilde{k}^{(II)}} e^{\imath k^{(I)} z}\hat{e}_y, \end{aligned} \tag{3.5}$$

or in spherical coordinates

$$\begin{aligned} \vec{E}^i &= e^{\imath k^{(I)} r\cos\theta}\left(\sin\theta\cos\phi\hat{e}_r + \cos\theta\cos\phi\hat{e}_\theta - \sin\phi\hat{e}_\phi\right), \\ \vec{H}^i &= \tfrac{\imath k^{(I)}}{\tilde{k}^{(II)}} e^{\imath k^{(I)} r\cos\theta}\left(\sin\theta\sin\phi\hat{e}_r + \cos\theta\sin\phi\hat{e}_\theta + \cos\phi\hat{e}_\phi\right). \end{aligned} \tag{3.6}$$

The boundary conditions which are needed are the continuity of the tangential components of the electric and magnetic fields across the sphere surface:

$$\left.\begin{aligned} E^{(I)}_{tang} &= E^{(II)}_{tang} \\ H^{(I)}_{tang} &= H^{(II)}_{tang} \end{aligned}\right\} \text{for } r = a, \tag{3.7}$$

where a is the radius of the sphere. In finding the complete electromagnetic field for the sphere the scattered ($\vec{E}^s$, $\vec{H}^s$) and internal ($\vec{E}^w$, $\vec{H}^w$) fields need to be determined. The total external electromagnetic field is then given by

$$\vec{E}_{ext} = \vec{E}^i + \vec{E}^s, \tag{3.8}$$

and a similar expression for the total external magnetic field. The internal fields are given by $\vec{E}^w$ and $\vec{H}^w$.

In spherical coordinates Maxwell's equations (3.1) become

$$\begin{aligned}
-\tilde{k}_1 E_r &= \frac{1}{r^2 \sin\theta}\left[\frac{\partial\left(rH_\phi \sin\theta\right)}{\partial\theta} - \frac{\partial\left(rH_\theta\right)}{\partial\phi}\right], \\
-\tilde{k}_1 E_\theta &= \frac{1}{r\sin\theta}\left[\frac{\partial H_r}{\partial\phi} - \frac{\partial\left(rH_\phi \sin\theta\right)}{\partial r}\right], \\
-\tilde{k}_1 E_\phi &= \frac{1}{r}\left[\frac{\partial\left(rH_\phi\right)}{\partial r} - \frac{\partial H_r}{\partial\theta}\right],
\end{aligned} \tag{3.9}$$

$$\begin{aligned}
H_r &= \frac{1}{r^2 \sin\theta}\left[\frac{\partial\left(rE_\phi \sin\theta\right)}{\partial\theta} - \frac{\partial\left(rE_\theta\right)}{\partial\phi}\right], \\
H_\theta &= \frac{1}{r\sin\theta}\left[\frac{\partial E_r}{\partial\phi} - \frac{\partial\left(rE_\phi \sin\theta\right)}{\partial r}\right], \\
H_\phi &= \frac{1}{r}\left[\frac{\partial\left(rE_\phi\right)}{\partial r} - \frac{\partial E_r}{\partial\theta}\right],
\end{aligned} \tag{3.10}$$

and the boundary conditions are

$$\left.\begin{aligned} E_l^{(I)} &= E_l^{(II)} \\ H_l^{(I)} &= H_l^{(II)} \end{aligned}\right\} \text{for } r = a \text{ and } l = \theta,\ \phi. \tag{3.11}$$

Equations (3.9) and (3.10) now need to be solved under the conditions of Equation (3.11). To do this the fields are divided into two linearly independent fields ($^e\vec{E}$, $^e\vec{H}$) and ($^m\vec{E}$, $^m\vec{H}$) which represent an *electric wave* (transverse magnetic wave) and a *magnetic wave* (transverse electric wave), respectively. The two fields must also be solutions of Equations (3.9) and (3.10); this is accomplished by applying the

conditions

$$ {}^{e}E_r = E_r, \quad {}^{e}H_r = 0, \quad \vec{\nabla} \cdot {}^{e}\vec{H} = 0, \tag{3.12} $$

to the electric wave and

$$ {}^{m}E_r = 0, \quad {}^{m}H_r = H_r, \quad \vec{\nabla} \cdot {}^{m}\vec{E} = 0, \tag{3.13} $$

to the magnetic wave. In doing this the fields can be expressed in terms of *Debye potentials* ($^{e}\Pi$ and $^{m}\Pi$) and the fields are given in terms of the potentials as

$$ \begin{aligned} E_r &= \frac{\partial^2 (r\,{}^{e}\Pi)}{\partial r^2} + \tilde{k}^2 r\,{}^{e}\Pi, \\ E_\theta &= \frac{1}{r}\frac{\partial^2 (r\,{}^{e}\Pi)}{\partial r \partial \theta} + \frac{k_2}{r\sin\theta}\frac{\partial (r\,{}^{m}\Pi)}{\partial \phi}, \\ E_\phi &= \frac{1}{r\sin\theta}\frac{\partial^2 (r\,{}^{e}\Pi)}{\partial r \partial \phi} - \frac{k_2}{r}\frac{\partial (r\,{}^{m}\Pi)}{\partial \theta} \end{aligned} \tag{3.14} $$

$$ \begin{aligned} H_r &= \frac{\partial^2 (r\,{}^{m}\Pi)}{\partial r^2} + \tilde{k}^2 r\,{}^{m}\Pi, \\ H_\theta &= \frac{1}{r}\frac{\partial^2 (r\,{}^{m}\Pi)}{\partial r \partial \theta} - \frac{k_2}{r\sin\theta}\frac{\partial (r\,{}^{e}\Pi)}{\partial \phi}, \\ H_\phi &= \frac{1}{r\sin\theta}\frac{\partial^2 (r\,{}^{m}\Pi)}{\partial r \partial \phi} - \frac{k_2}{r}\frac{\partial (r\,{}^{e}\Pi)}{\partial \theta}. \end{aligned} \tag{3.15} $$

Both Debye potentials are solutions of the wave equation

$$ \nabla^2 \Pi + \tilde{k}^2 \Pi = 0, \tag{3.16} $$

and the boundary conditions require that the values

$$ \tilde{k}_1 r\,{}^{e}\Pi, \quad k_2 r\,{}^{m}\Pi, \quad \frac{\partial (r\,{}^{e}\Pi)}{\partial r}, \quad \frac{\partial (r\,{}^{m}\Pi)}{\partial r}, \tag{3.17} $$

are continuous over the sphere's surface.

The results presented so far are general to any incident wave. All that remains is solving Equation (3.16) for an incident plane-wave under the boundary conditions.

Born and Wolf show that a general solution to the wave equation in spherical coordinates is

$$r\Pi = \sum_{l=0}^{\infty} \sum_{m=-l}^{l} \left[c_l \psi_l(kr) + d_l \chi_l(kr)\right] \left[a_m \cos(m\phi) + b_m \sin(m\phi)\right] P_l^m(\cos\theta), \quad (3.18)$$

where a_m, b_m, c_l, and d_l are constants, ψ_l and χ_l are the Ricatti-Bessel functions of the first and second kind respectively, and P_l^m is the associated Legendre function. In the derivation of the electromagnetic fields the external medium is not assumed to be absorbing (the external index of refraction is purely a real number). This results in the following values (determined from Equations (3.1), (3.2) and (3.3))

$$\begin{aligned}
k_1^{(I)} &= \imath \frac{2\pi}{\lambda} n^{(I)^2}, \\
\tilde{k}_1^{(II)} &= \imath \frac{2\pi}{\lambda} \tilde{n}^{(II)^2}, \\
k_2^{(I)} &= k_2^{(II)} = \imath \frac{2\pi}{\lambda}, \\
k^{(I)} &= \frac{2\pi}{\lambda} n^{(I)}, \\
\tilde{k}^{(II)} &= \frac{2\pi}{\lambda} \tilde{n}^{(II)},
\end{aligned}$$

where λ is the wavelength in vacuum. The complex index of refraction of the sphere relative to the surrounding medium is defined as

$$\tilde{n} = \frac{\tilde{n}^{(II)}}{n^{(I)}}. \quad (3.19)$$

As well, the dimensionless size parameter (q) is used and defined as

$$q = k^{(I)} a = 2\pi n^{(I)} \frac{a}{\lambda}. \quad (3.20)$$

Based on the general solution (3.18) and assuming an incident plane-wave, the fol-

lowing Debye potentials for the internal and scattered fields are

$$\begin{aligned} r^e\Pi^w &= \frac{1}{(\tilde{k}^{(II)})^2}\sum_{l=1}^{\infty} {}^e\tilde{A}_l\psi_l(\tilde{k}^{(II)}r)P_l^1(\cos\theta)\cos\phi, \\ r^m\Pi^w &= \frac{\imath}{\tilde{k}^{(II)}k_2^{(II)}}\sum_{l=1}^{\infty} {}^m\tilde{A}_l\psi_l(\tilde{k}^{(II)}r)P_l^1(\cos\theta)\sin\phi, \end{aligned} \tag{3.21}$$

$$\begin{aligned} r^e\Pi^s &= \frac{1}{(k^{(I)})^2}\sum_{l=1}^{\infty} {}^e\tilde{B}_l\tilde{\xi}_l(k^{(I)}r)P_l^1(\cos\theta)\cos\phi, \\ r^m\Pi^s &= \frac{\imath}{k^{(I)}k_2^{(I)}}\sum_{l=1}^{\infty} {}^m\tilde{B}_l\tilde{\xi}_l(k^{(I)}r)P_l^1(\cos\theta)\sin\phi, \end{aligned} \tag{3.22}$$

where χ_l has been suppressed from the internal field since it is infinite at the origin and $\tilde{\xi}_l = \psi_l - \imath\chi_l$ is used for the scattered field since it represents an outward traveling wave. With an expression for the Debye potentials the electromagnetic fields can be solved for by substituting Equations (3.21) and (3.22) into Equations (3.14) and (3.15). The unknown constants $\tilde{A}$ and $\tilde{B}$ are solved for by substituting the Debye potentials into the boundary conditions (3.17). The results of this are given in Appendix A. With the development of the theory used to determine the electromagnetic fields around a micro-sphere, the attention is now turned to the implementation of this theory into calculation.

3.2 Method of Calculation

There are several different approaches to determine the electromagnetic fields around a micro-particle when irradiated by a plane wave. In the previous section the original derivation performed by G. Mie was presented. Another method is called the T-Matrix method [38] and it involves the solution of the fields around an axisymmetric particle irradiated by a plane wave. With this method, the electromagnetic fields are expanded in terms of the vector spherical functions and then the expansion coefficients are determined. In the case of a spherical particle, both the T-Matrix and Mie's theory

result in equivalent expressions for the fields. The computer codes used in this work were adapted from the codes of Barber & Hill [38] where the electromagnetic field expressions are determined from the T-Matrix approach. However, they are the same as those given in Appendix A and Mie's theory was presented since it provides a simple, concise derivation. As well, Mie's approach is easily adapted to calculate the electromagnetic fields in the case of a non-plane wave incident field.

The equations of the fields are relatively straight forward to calculate and do not require any advanced numerical techniques. Both the Ricatti-Bessel functions and the associated Legendre polynomials were calculated using recursion techniques, and the results proved to be fine for the required accuracy. A consideration in the calculation of the fields is the order of the calculation. The expressions for the fields do involve a sum over an infinite number of terms. This sum would be time consuming to perform and is not necessary since a calculation on a computer is limited in accuracy. Therefore, to speed up the calculation and still determine a correct field, the sum is carried out over a number of terms which result in convergence of the calculated field. According to references [38,39], the number of terms required for convergence (n_c) is

$$n_c = q + 4.05q^{1/3} + 2. \tag{3.23}$$

Equation (3.23) is adequate for smaller magnitudes of the index of refraction but for larger magnitudes of the index of refraction—around 2 or more—the number of terms should be increased. A good starting point is [38]

$$n_c = |\tilde{n}^{(II)}q|. \tag{3.24}$$

The change in the number of convergence terms can also affect the calculation of the special functions; the starting points and values for recursion may need to be altered. In the implementation of the calculations the number of terms calculated

for the electromagnetic fields and special functions are always varied to check for convergence.

In implementing this method two programs have been created (BHBOTH and BHBOTHM); they both calculate the intensity surrounding the sphere using

$$I = \vec{E} \cdot \vec{E}^*, \tag{3.25}$$

in a plane that is chosen by the user. The index of refraction of the medium surrounding the sphere is set to 1 and the sphere's index is entered by the user. As well, the wavelength of the incident light and the sphere's size are entered into the program. The difference between the programs is that BHBOTH uses Equation (3.23) for convergence while BHBOTHM uses Equation (3.24) plus a user entered correction to this initial number of convergence terms. Therefore, BHBOTH may be used for dielectric micro-spheres where the internal index of refraction is small and BHBOTHM may be used for any type of micro-sphere (i.e. any magnitude of the index of refraction).

The validity of the results of the computer programs has been examined for the dielectric case. Intensity distributions around spheres produced from these programs have been compared with distributions from references [7,9,40] where the same parameters were used in the calculations. The results all were qualitatively the same. In other words, the appearance of the distributions (for example, the location of the maximum intensities or the location of interference fringes) were identical. As well, the values of the maximum enhancements were the same. For the metal spheres the benchmarking was not so straightforward. This is because calculations of the intensity enhancements around metal micro-particles have not been published by an independent research group. However, calculations of the intensity above metallic nano-boxes have been performed [41, 42] and the intensity distributions appear to have similarities—there is a "shadow" behind the metal nano-particle and strong in-

terference fringes in front of it (see Figure 3.7). The results also show properties of the electromagnetic fields around metal particles with a size comparable to the wavelength of light. One property is that the field is a maximum on the surface of the particle and decays rapidly with distance away from the surface. As well, the calculations show that the strength of the field inside the particle also decays rapidly. It is therefore expected that the intensity distributions around micro-spheres which are produced by the computer programs are valid.

3.3 Calculated Fields

In this section some results of the calculations will be presented. The focus is mainly on trends of the fields based on the micro-sphere size parameter for two types of materials: dielectrics and metals. The two materials have distinctly different indices of refraction and therefore, the nature of the light around the spheres will be quite different. In both cases, the wavelength of light used in the calculations was 800 nm.

3.3.1 Dielectric Micro-Spheres

In this current work the removal of 2.5 μm glass micro-spheres has been examined and Figure 3.2 is the result of the calculation of the intensity surrounding this micro-sphere. Figures 3.2(a) and 3.2(b) are calculations in the plane along the axis where the incident plane-wave polarization is parallel and perpendicular to the calculation plane, respectively. Similarly, Figure 3.2(c) is in the plane directly below the sphere, or in other words, the plane of the surface that the micro-sphere lies on.

The parallel and perpendicular plots show the focusing of the incident light by the micro-sphere. Semi-circular interference fringes are easily seen and their focus is on the back surface of the micro-sphere. The intensity of the field on the back

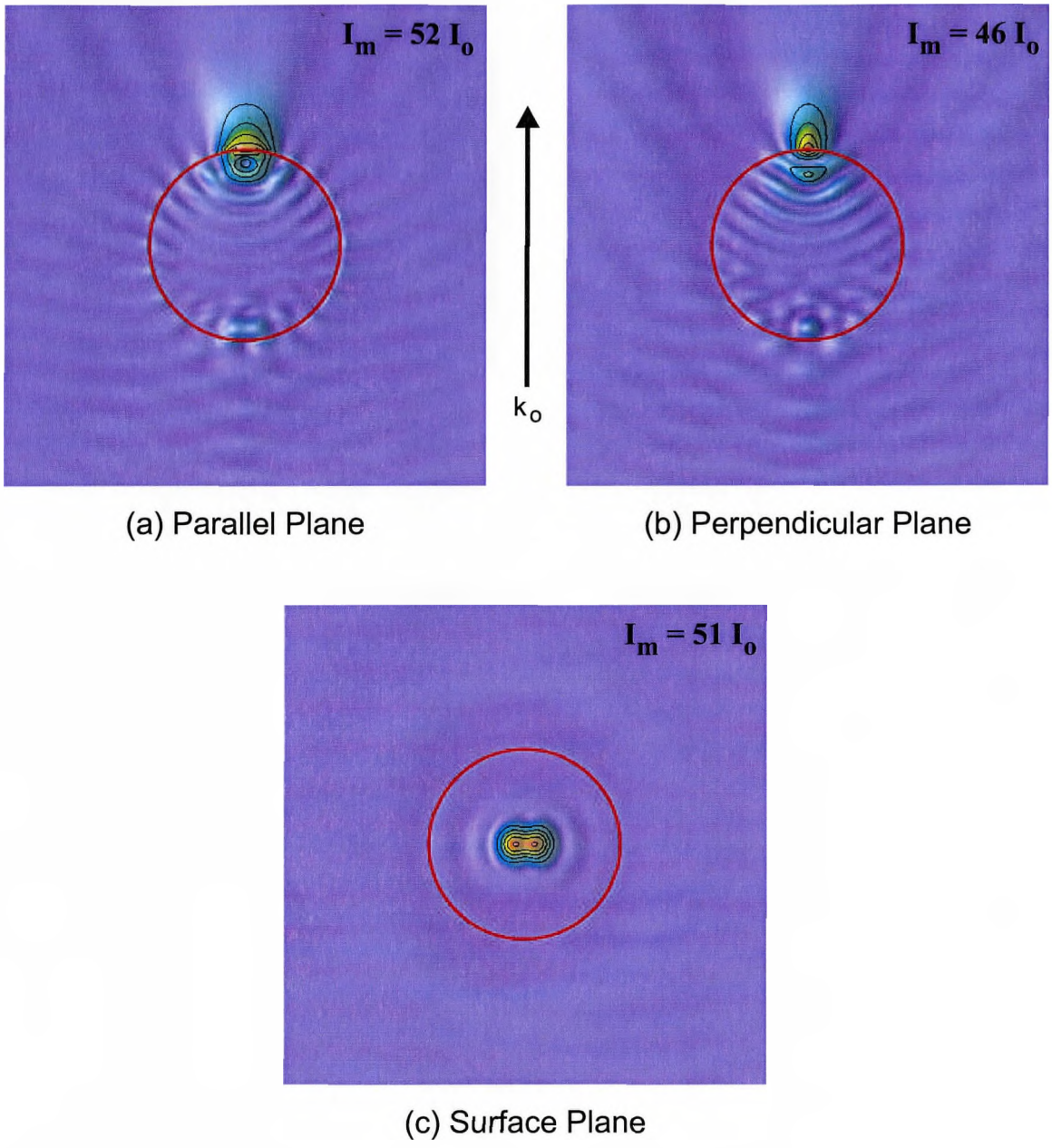

Figure 3.2: Intensity distributions for a 2.5 μm glass micro-sphere ($n = 1.5$) in the (a) plane of the incident polarization, (b) plane perpendicular to the incident polarization and (c) the plane directly below the micro-sphere. The red circles denote the size and position of the micro-sphere, I_m corresponds to the maximum intensity in the calculated plane, and the contour interval for all the figures is $10I_o$.

of the micro-sphere is roughly 50 times the incident intensity. Another interesting aspect of this calculation is the region into which the light has been focussed. This can be easily seen in the surface plane where the width of the light confinement region is approximately a third of the micro-sphere's diameter. This means that, approximately, the light is focussed into a region with a width that is approximately the same as the wavelength.

The size of the micro-sphere is an important parameter to the distribution of the light. As this parameter changes the distribution will also change. Figure 3.3 shows the intensity distribution around a 400 nm glass micro-sphere. Again, the light has been focussed into a region that is roughly on the scale of the wavelength but this time the intensity enhancement is much less. This can been seen in the surface plane calculation where there is an enhancement of only about 2 times the incident intensity. The perpendicular plane also shows that the focus spot has moved farther into the sphere. The last two observations actually appear to be general results for dielectric micro-spheres. The larger the size of the micro-sphere, the farther away from the sphere the focus is located and the intensity enhancement is greater. This can be seen in Figure 3.4 which is an intensity calculation directly along the z-axis. However, for the smaller sub-wavelength spheres, the maximum intensity may not be along this axis. This can be seen in the parallel plane where there is an enhancement of approximately three times the incident intensity to the sides of the sphere.

Another parameter that affects the fields is the internal index of refraction. For dielectrics the imaginary part can usually be neglected with little loss of accuracy and this is certainly true in the current case; there will be little absorption by dielectric micro-spheres with sizes comparable to the wavelength. The effect of the index can be seen in Figure 3.5 where a larger index results in a greater enhancement of the

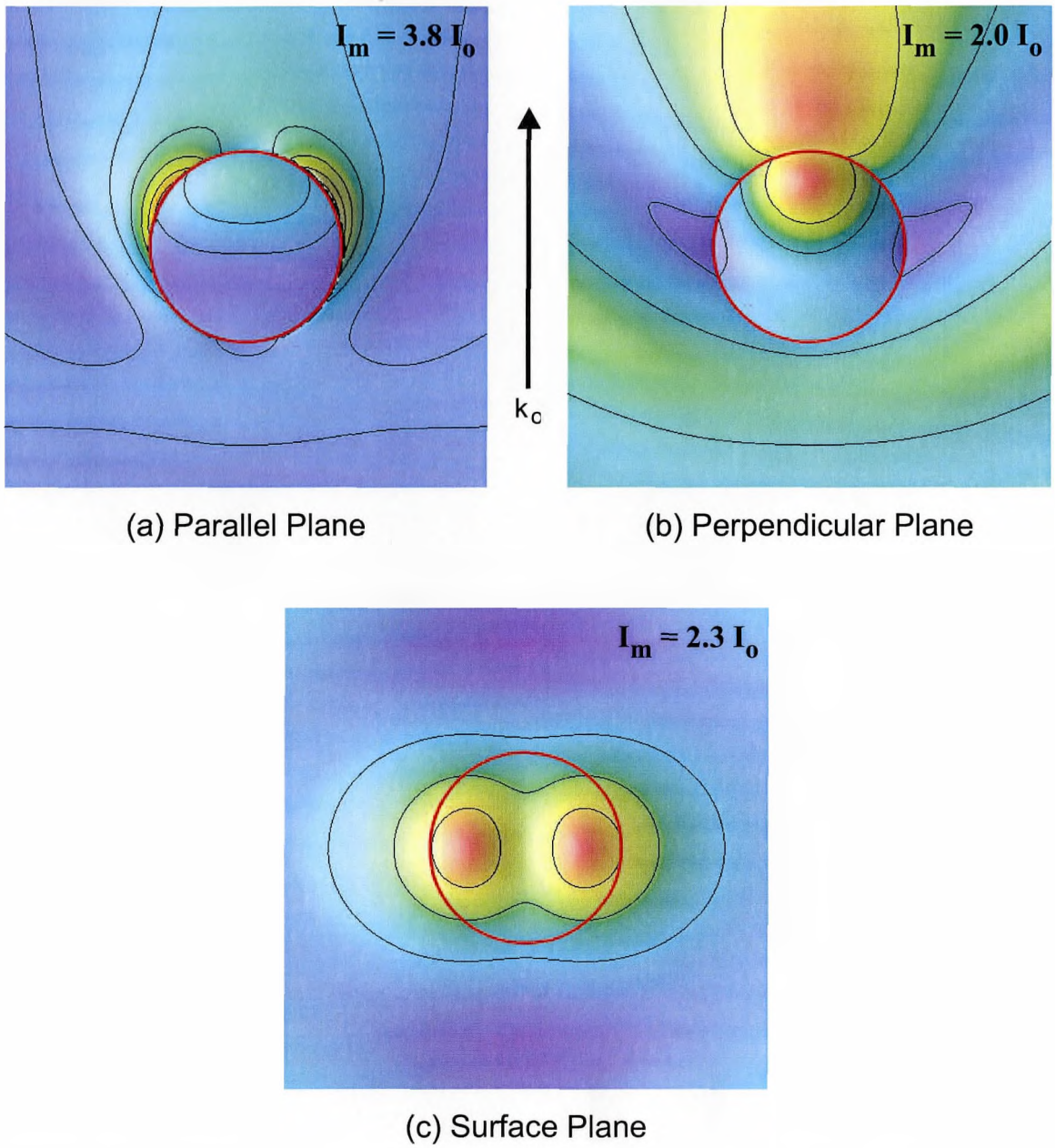

Figure 3.3: Intensity distributions for a 400 nm glass micro-sphere. The maximum intensity has significantly decreased from the 2.5 μm case and this maximum is located to the sides of the sphere. The contour interval for all the figures is $0.5I_o$ but in (a) and (b) the first contour is $1.0I_o$ and in (c) it is $0.5I_o$.

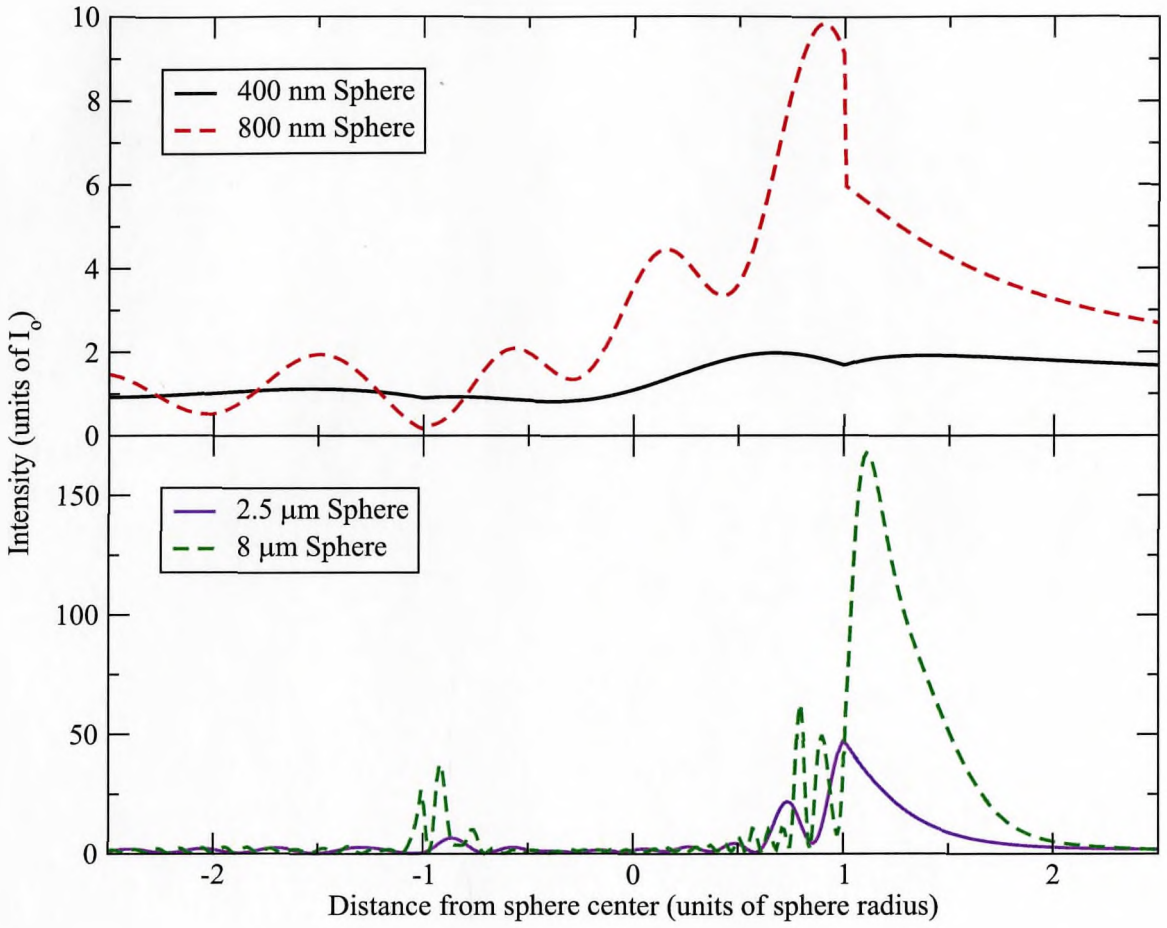

Figure 3.4: The effect of the size on the axial intensity distributions of a glass micro-sphere. The incident plane-wave moves from left to right. As the size is increased the maximum intensity increases and moves further behind the micro-sphere.

field. If the index was smaller, the opposite would be true.

The results of these calculations show that dielectric micro-spheres act like small lenses. The analog to larger lenses certainly holds for spheres which are significantly larger than the wavelength of light. However, when the size becomes smaller than the wavelength, the ray-optic view of the lens does not hold well. The behaviour of the light field does depend strongly on the plane of interest and maximum intensity enhancements may lie to the sides of the micro-sphere as opposed to being along the axis.

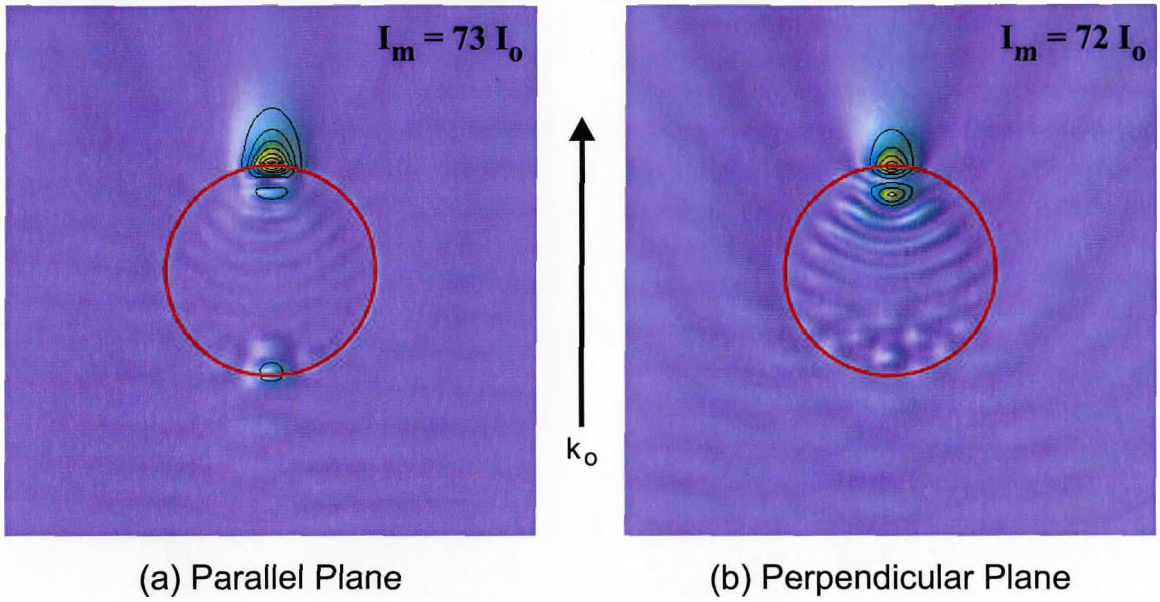

Figure 3.5: Intensity distributions for a 2.5 μm polymer micro-sphere ($n = 1.6$). The effect of increasing the index of refraction is an increase in the intensity enhancement. The contour interval for both figures is $10I_o$.

3.3.2 Metallic Micro-Spheres

When metallic materials are examined the results become quite different. This could be expected since dielectrics generally have negligible imaginary parts of the index of refraction. However, for a metal this imaginary part can be significantly larger than the real part. This results in high surface reflectivities and very short skin depths of transmitted light. It is expected then that the same focussing of the incident light by the micro-sphere which was calculated in the dielectric case will not occur. One may then believe that there will be no intensity enhancements behind the micro-spheres. Yet the calculations performed on metallic micro-spheres lead to some interesting results.

Figure 3.6 is the field around a 2 μm silver micro-sphere with an index of refraction of $0.27 + i5.79$ at 800 nm. As is to be expected, the field inside the sphere

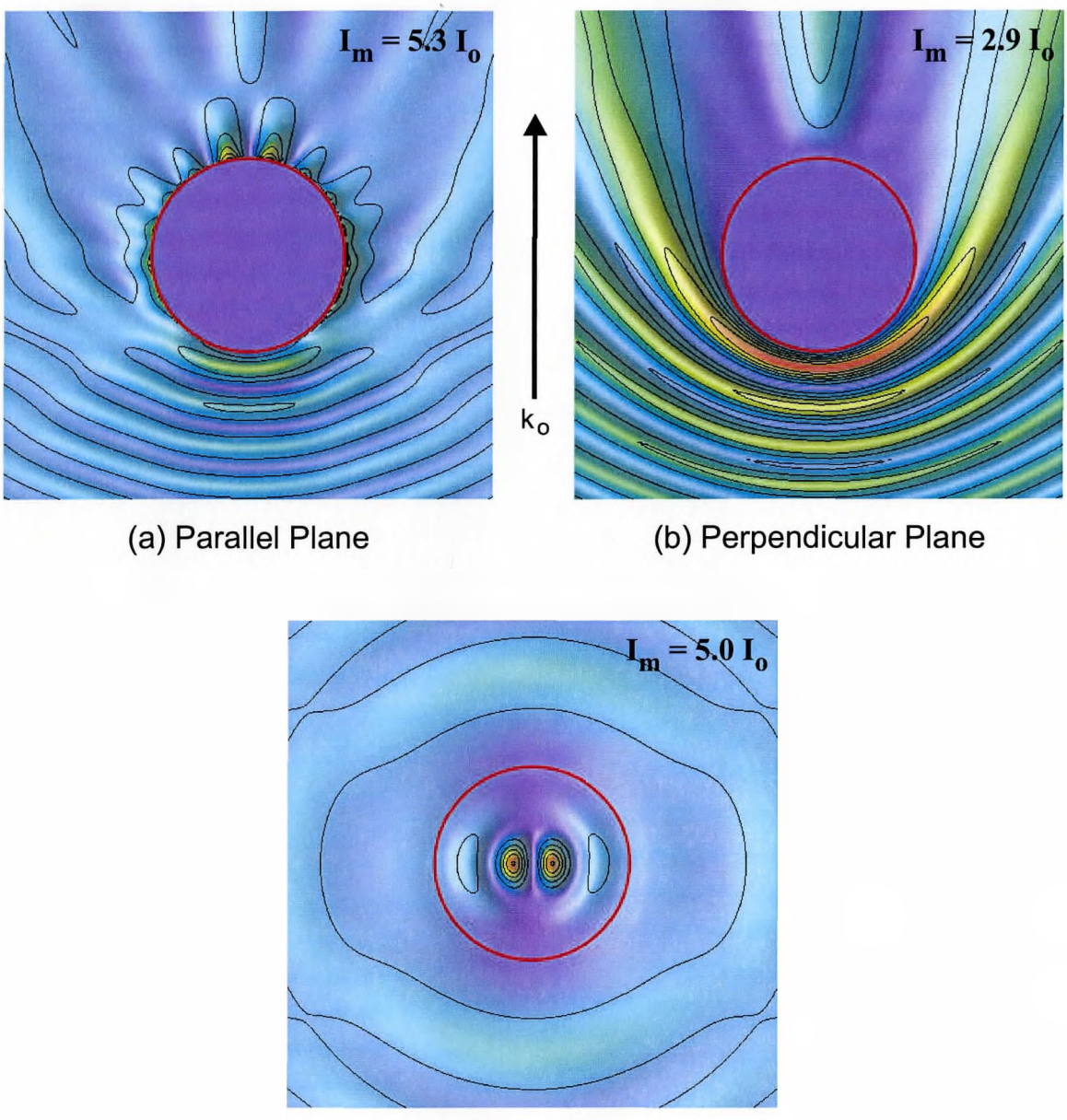

Figure 3.6: Intensity distributions for a 2 μm silver micro-sphere. There is actually an intensity enhancement below the micro-particle for the parallel plane, but in the perpendicular plane there is a "shadow" behind the sphere. The contour interval for (a) and (b) is $1.0I_o$ while for (c) it is $0.5I_o$.

drops very rapidly and is only non-zero near the surface. The perpendicular plane does show a distribution that might be expected; there is no intensity directly behind the sphere but the intensity increases as the distance behind the sphere increases, presumably a result of diffraction around the sphere. However, in the parallel plane there is an electromagnetic field behind the sphere which decays quite rapidly with distance away from the surface. This is a result of surface waves which travel along the surface of the sphere. The back plane shows that on the surface there can be an intensity enhancement below the sphere. The intensity enhancements in this case are low compared to the dielectric case; for this sphere there is an enhancement of about 5 times the incident intensity.

Figure 3.7 is the same calculation for the intensity distribution around a 400 nm silver micro-sphere. Here there is a similar behaviour to Figure 3.6 with a basically zero intensity inside the sphere. In the parallel plane, the region where the intensity is mainly located is on the sides and this is similar to the dielectric case. There is an increase of the intensity enhancement: it is roughly 11 times the incident intensity. In the surface plane there is also a more significant intensity enhancement than in the case of the 2 μm micro-sphere. The intensity enhancement is actually greater than what was calculated for the dielectric case with the same size of micro-particle. Another interesting result is that, in the surface plane, the two peaks below the sphere are separated by a significant distance, whereas in the dielectric case there is more intensity between the peaks. This applies to both micro-sphere sizes calculated.

For the silver micro-sphere calculations there are some interesting results. While the electromagnetic fields depend on the index of refraction that is specific to the material, and therefore do not hold for all metals, they are representative of what occurs for a metal micro-sphere. The main intensity enhancements are located on

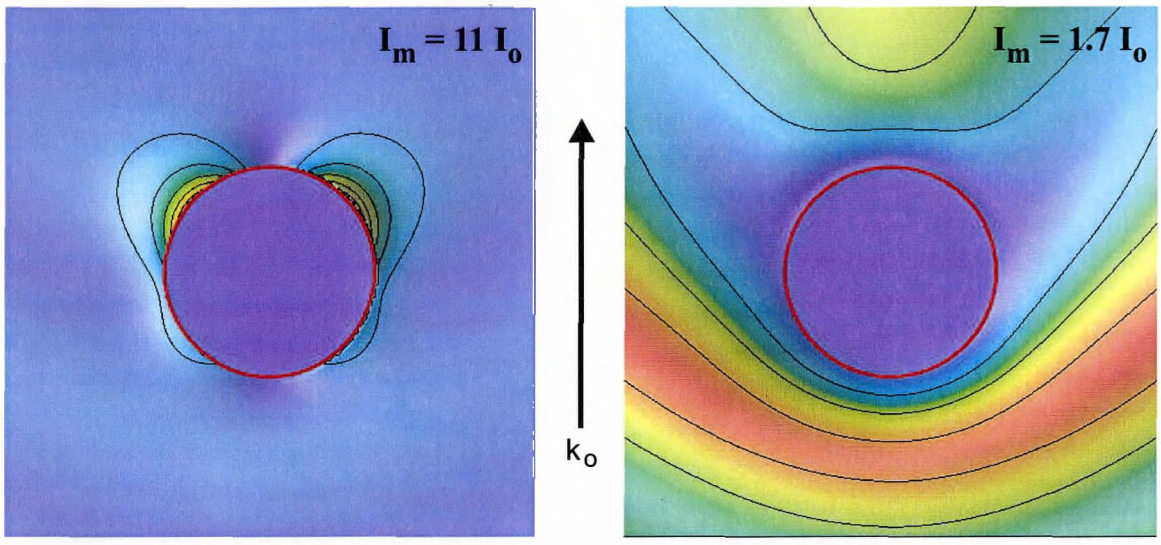

(a) Parallel Plane

(b) Perpendicular Plane

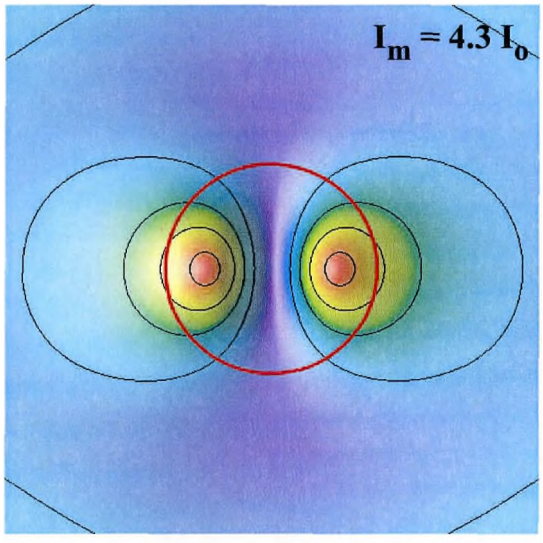

(c) Surface Plane

Figure 3.7: Intensity distributions for a 400 nm silver micro-sphere. The maximum intensity increases in relation to the larger silver micro-sphere and in (a) it can be seen that this maximum is actually located to the sides of the sphere. The contour interval for (a) is $2.0I_o$, for (b) it is $0.5I_o$ and for (c) it is $1.0I_o$.

the sphere surface and decay rapidly with distance from the surface. Polarization is also very important resulting in parallel polarization giving the maximum intensity enhancements. While this is immaterial for an isolated sphere where the geometry is completely symmetrical, for a sphere on a surface the intensity on the surface will depend significantly on the orientation of the polarization and incident beam direction. Finally, contrary to the dielectric case, as the micro-particle size decreases, the intensity enhancement will increase (a maximum enhancement of 20 times is achieved for a silver micro-sphere with a diameter of 100 nm; then the enhancement does decrease with decreasing micro-sphere size).

3.4 Calculation Shortcomings and Future Developments

The method of calculation that has been presented and used in the previous sections does give results which elucidate the properties of electromagnetic fields around micro-spheres. However, there are some shortcomings which may significantly change the electromagnetic field's nature. The two primary shortcomings are that the incident beam was taken to be a plane wave instead of a Gaussian beam and also that the effect of the surface was ignored. These deficiencies of the calculation and future developments which might eliminate these concerns will now be discussed.

The first problem is the choice of incident beam. Experimentally, a Gaussian beam is used and this beam has a different waveform and intensity profile than a simple plane-wave. However, if the beam waist is significantly larger than the particle size, there may be little problem with the intensity distribution. As well, at the focus spot of a tightly focussed beam, the wavefronts can essentially be described by plane-waves [43]. Therefore, in the case where the micro-sphere is located at or near the

focus of the beam and its size is much smaller than the waist, the use of an incident plane-wave in the calculations should produce realistic intensity distributions. As the situation deviates from these conditions the effect of the Gaussian beam will become more pronounced. The intensities can still be solved for in this case using a generalized Mie theory solution which can be calculated for an arbitrary incident field. This method is outlined by Barton *et al.* in reference [40]. For the current work, this method has been attempted but has not yet produced useful results.

A potentially more severe limitation on the calculations is that they are performed in free-space. That is, they do not take the surface which the micro-sphere lies on into account. The effect of the surface may be insignificant for a dielectric substrate with an index of refraction close to the surrounding medium, but in the case of a metal with high surface reflectivity, the field distribution may change significantly. Unfortunately, accounting for the surface cannot be implemented into Mie theory due to the planar substrate surface. However, there does exist a more powerful technique for electromagnetic field calculations which allows for non-spherical shapes and is called Green's dyadic technique [44–49]. For future calculations this technique would be employed, but for the current work it was not.

There are some smaller concerns with the calculations. One is that the calculations only consider monochromatic light. The nature of short pulses is that they have reasonably large bandwidths (the two femtosecond lasers used in our lab produce pulses with bandwidths of 10 nm and 40 nm) and therefore, there may be small effects to the electromagnetic fields. As well, the calculation ignores effects of non-linearity which might be a concern for the high intensities produced by femtosecond lasers. However, it is believed that these effects are rather insignificant for the present purpose.

Chapter 4

Experimental Details

In the previous chapters the theory behind the current work was discussed. As mentioned previously, a complete scientific investigation should also involve some verification of the theory. The theory presented in Chapter 2 consists of several possible micro-particle removal mechanisms and the experimental efforts should elucidate the appropriate removal mechanism. For the current work an experimental setup was used to determine the threshold pulses fluences needed to move the micro-particles. Subsequent analysis of the surfaces after irradiation was also performed and together with the thresholds the mechanism for micro-particle movement on substrate surfaces was examined.

This chapter starts with a description of the experimental apparatus that has been employed to remove the micro-particles. This description involves the design of the apparatus and also the way each component was used together in the process of removing micro-spheres from surfaces. The chapter then discusses the experimental methods that were employed in the removal of the micro-particles. This includes the preparation, process of removal and subsequent analysis of the micro-particles and substrates.

4.1 Experimental Apparatus

The experimental apparatus that was employed can be divided into two major components: the laser source and the micro-particle removal setup. For these experiments an ultrafast laser system was used and the removal setup consisted of optical components (such as a microscope objective) which allowed the selective control of tightly focussed, individual laser pulses in irradiating a substrate surface containing micro-particles. A necessary condition was that there be a method to target single micro-particles where particle–particle interactions would not be present. As well, the removal of the micro-particles needed to be observed and correlated with the pulse fluences at which this occurred.

4.1.1 Ultrafast Laser System

The ultrafast laser system that was employed in these experiments was a Ti:Sapphire system which is able to produce pulse lengths as short as 120 fs. One can think of the laser system consisting of two main components: a Ti:Sapphire oscillator (Spectra Physics: Tsunami) and a Ti:Sapphire regenerative amplifier (Spectra Physics: Spitfire). The Tsunami is a mode-locked Ti:Sapphire oscillator which outputs around 80 fs pulses with a bandwidth of 10 nm at a repetition rate of about 82 MHz. The output wavelength of the Tsunami is adjustable but for the present purposes it was 800 nm and the output power of the Tsunami can be nearly as high as 1 W. While the Tsunami provides short pulses, the pulse energy is quite low and the repetition rate quite high. Therefore, a regenerative amplifier is used to amplify the pulse energies and lower the pulse repetition rate (this is adjustable from around 10 Hz to 1 kHz for the Spitfire). This is done in a multi-pass cavity with a Ti:Sapphire crystal which is pumped by a frequency-doubled, Q-switched Nd:YLF laser (Spectra Physics: Merlin)

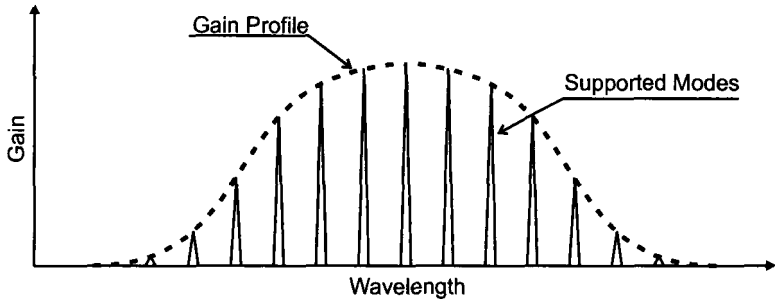

Figure 4.1: Representation of the longitudinal modes and gain profile for an ultrafast laser. The gain medium of the laser is able to amplify many longitudinal modes. The more modes that are amplified and locked, the shorter the duration of the mode-locked pulse.

and can output 120–130 fs pulses with an energy of up to 300 μJ. For some experiments an updated version of this system was used which can output 45 fs pulses (they are also variable in pulse length) with a bandwidth of 40 nm. Some details behind the method used to generate and amplify femtosecond pulses will be further examined.

Femtosecond Pulse Generation

The creation of ultrashort laser pulses is achieved through mode-locking. This is a method in which multiple longitudinal modes of the laser cavity are forced to "oscillate" in phase with each other. The result is a short laser pulse that oscillates in the cavity and the outputted pulse repetition rate is equal to the travel time of the pulse in the cavity. Figure 4.1 is a representation of the gain profile for a laser cavity. The longitudinal modes of the cavity are equally spaced and, provided the gain profile is broad enough, there are several modes that lie within the profile of the laser gain medium. These modes will be amplified in the laser and mode-locked to provide the short pulses. Basically, the more modes that are locked, the shorter the pulse. This makes solid state lasers like Ti:Sapphire desirable for ultrashort pulse generation since the gain medium has a broad gain profile.

If the modes in an ultrafast laser are not intentionally modified, they will operate in the c.w. regime. Therefore, a method of mode-locking needs to be employed and there are several ways of doing this [50]. In the Tsunami the method of self-locking of the modes is used and this is achieved through Kerr lens mode-locking (KLM) [50]. This method relies on the non-linear nature of the Ti:Sapphire crystal with an index of refraction given by

$$n(I) = n_o + n_2 I, \tag{4.1}$$

where I is the light intensity. Due to the Kerr effect (represented by the n_2 term), an index profile across the laser beam results which leads to self-focussing [50]; in other words, the beam is focussed in the gain medium to a smaller width. How this may lead to self-locking is shown in Figure 4.2, which is a depiction of the standard design of a KLM Ti:Sapphire laser cavity. When the modes operate in the c.w. regime the intensities are not large enough for self-focussing. The aperture is set to a width smaller than the beam width of these modes. Therefore, the gain of these modes is greatly diminished. If the modes are locked, then self-focussing is realized and the aperture will not significantly affect the pulse's gain. In this manner, the laser cavity is designed to selectively prefer mode-locked operation, but it does not guarantee initiation of mode-locking (c.w. operation is still the "natural" mode). Mode-locking is achieved by introducing a brief intensity enhancement (generally by quickly changing the cavity length) which will lead to self-focussing and stable mode-locked operation of the laser [50].

The nature of short pulses is that they must have large bandwidths. This can lead to significant dispersion of the pulse which cannot be ignored. One form of dispersion that occurs is group velocity dispersion (GVD) [51]. This is due to the wavelength variation of the index of refraction and can result in pulse broadening

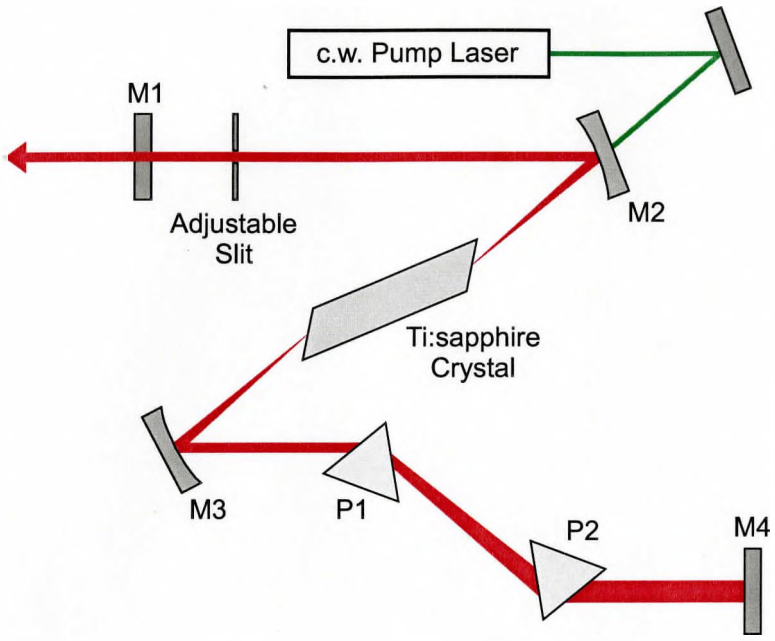

Figure 4.2: Diagram of a standard Ti:Sapphire laser cavity. The laser cavity is the region between mirrors M1 (output coupler) and M4 and co-linear pumping of the Ti:Sapphire crystal is achieved through M2. The adjustable aperture is placed next to M1 and results in large losses for c.w. operating modes. Dispersion compensation is achieved in-cavity by placing prisms P1 and P2 between M3 and M4 which results in pulse compression.

(positive GVD) or shortening (negative GVD). Most materials in the visible regime show positive GVD [50] and, therefore, result in a broadening of the pulse. This can be partially compensated for by using a prism compressor in the laser cavity as shown in Figure 4.2. Another form of dispersion is called self-phase modulation (SPM) and results from the non-linear nature of the index of refraction [52]. Equation (4.1) applies to spatial intensity distributions to give self-focussing and it also applies to temporal intensity variations leading to SPM. The index changes which the pulse experiences leads to a shortening of its duration. It is through the equilibrium of the effects of GVD and SPM that the pulse reaches its steady-state pulse length [50].

Femtosecond Pulse Amplification

It may be necessary to amplify the energies of the pulses that are created in the Tsunami. As well, it may also be necessary to significantly decrease the repetition rate of the outputted pulses. In the current work, this is perhaps the more important reason an amplifier is used since the pulse energies produced by the Tsunami are nearly sufficient for removal, but the repetition rate is too high to selectively choose a single pulse. The amplifier used in the current work employs chirped pulse amplification (CPA) [50]. A schematic representation of CPA is shown in Figure 4.3. If a femtosecond pulse were amplified, the resulting pulse intensities would lead to damage to the optical components in the amplifier. Therefore, using CPA, the pulses are first stretched in time to lower the peak intensities significantly. The pulse is then amplified in a multi-pass Ti:Sapphire cavity and the pulse output rate can be selectively chosen. As well, the number of pulse cavity passes can be chosen to output pulses with the maximum amplification. The resulting pulse intensities are still not large enough to result in optical damage and after amplification the pulses are compressed to lengths nearing their initial pulse lengths. In the pulse stretching and compression stages gratings are used and the two methods are analogous. Stretching is achieved by making the red frequencies of the pulse travel a shorter distance in the stretcher, and in the compressor the blue frequencies travel a shorter distance. After femtosecond pulse generation and amplification, the system used in this study is able to produce 120–130 fs pulses with energies up to 300 μJ.

Femtosecond Pulse Characterization

It is also important to characterize the properties of the pulses. Two main properties are of interest in the current work: the pulse energy and the pulse length. The pulse

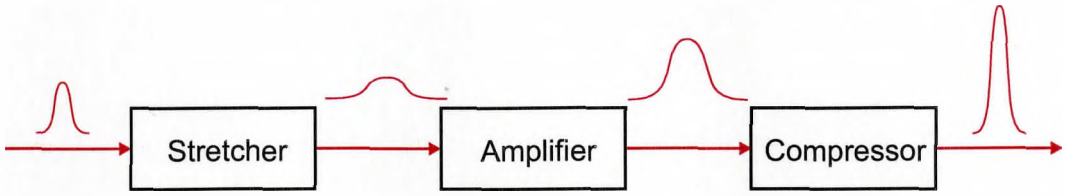

Figure 4.3: An overview of the method of chirped pulse amplification. The initial pulse length is lengthened first in a pulse stretcher using gratings. The resultant pulse is then amplified in the multi-pass Ti:Sapphire laser cavity until maximum amplification is achieved. Finally, the pulse is compressed to nearly its original length using a series of gratings.

energy can simply be determined by measuring the beam power with an optical power meter. Then, knowing the pulse repetition rate, the energy of a single pulse can be determined. Determination of the pulse length is not as straight forward since it cannot be done by electronic methods due to the short pulse durations. In order to measure the pulse length, an optical method is employed which involves the use of a second-order autocorrelator [50]. Figure 4.4 is a diagram of the autocorrelator used and shows that it is based on a Michelson interferometer. The initial pulse is split equally by the beamsplitter. One pulse travels through the fixed-length reference arm and the other through the delay arm. The length the pulse travels in the delay arm is variable and results in a time delay between the reference pulse ($I(t)$) and the delayed pulse ($I(t+\tau)$ where τ is the time delay). The pulses are then recombined at the non-linear crystal where the autocorrelation intensity (I_2) is given as

$$I_2(\tau) = \int_{\infty}^{\infty} I(t)I(t+\tau)dt. \tag{4.2}$$

The combined pulse intensity can lead to frequency doubling and the intensity of the second harmonic produced is measured by a photodetector. The photodetector voltage is proportional to the second harmonic intensity and this is proportional to the autocorrelation intensity. The autocorrelation intensity strongly depends on the time delay and by varying τ, the intensity profile of the pulse may be determined. By

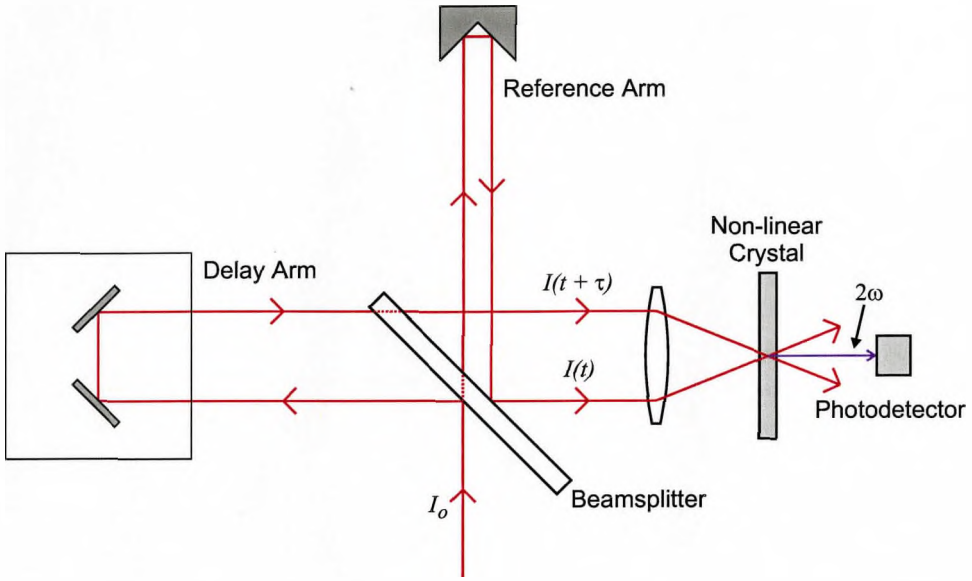

Figure 4.4: Diagram of a second-order autocorrelator based on a Michelson interferometer. The incident pulse energy is split 50:50 by the beamsplitter and one pulse travels through a static length reference arm and the other through a variable length delay arm. The pulses are recombined in a non-linear crystal and second harmonic generation occurs proportional to the recombined pulse intensity. The second harmonic beam (2ω) is detected by a photodiode and the voltage is proportional to the autocorrelation of the two pulses.

fitting an assumed Gaussian intensity profile to the measured profile the pulse length can be determined.

4.1.2 Micro-Particle Removal Setup

The apparatus that was used to remove the spheres is shown in Figure 4.5. The Spitfire output is directed by a series of dielectric mirrors to a microscope objective. The microscope objective then focusses the pulses onto the substrate below. By using a microscope objective the pulses can be tightly focussed. Both 5x and 10x objectives have been used and they give beam waists (ω_o) of 4.7 μm and 3.2 μm, respectively. It is with these tightly focussed beams that individual micro-particles can be targeted and removed. In performing the experiments, it is important that

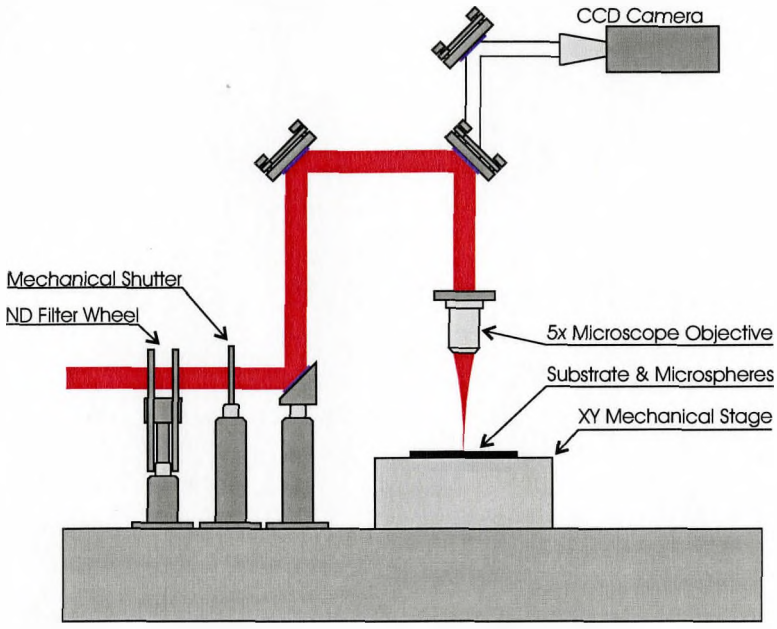

Figure 4.5: Diagram of the experimental setup used in the micro-particle removal.

one is able to perform the removal of particles multiple times as well as being able to observe the particle movement or removal. The ability to repeat the removal of many micro-particles is achieved, quite simply, by mounting the substrate onto a two-axis mechanical stage. This stage can be controlled by computer to translate new, unirradiated particles into the laser beam focus. Visualization of this process is done by a CCD camera (as shown in Figure 4.5) which is also focused onto the substrate surface by the microscope objective. The camera is connected to a monitor and the beam focus is marked by a transparent cross-hair template on the monitor. This is not only useful in targeting micro-particles, it is also used to determine if a micro-particle was removed and the approximate distance the particle traveled.

Besides the targeting and observation of micro-particles, the experimental setup consists of components to control the laser beam. Specifically, a method to select individual pulses and manipulate pulse energies is required. Individual pulse selection is performed with a mechanical shutter which is synchronized with the Spit-

fire output. When performing an experiment, the Spitfire is set to 10 Hz so that the shutter response time will guarantee only single pulse transmission (the shutter is opened 50 ms after the Spitfire trigger signal for approximately 100 ms). As with the mechanical stage, the shutter is controlled by the user on a computer. After the user tells the computer to open the shutter, the computer will wait until receiving the next timing signal from the Spitfire before opening the mechanical shutter. The pulse energy—or pulse fluence—is controlled by two main components: a half-wave plate plus linear polarizer combination as well as a neutral density filter wheel. The pulse energies achieved in the Spitfire are greatly in excess of what is needed to remove the particle. The majority of this energy is removed by the half-wave plate–polarizer combination. The half-wave plate is mounted in a rotating mount which allows the incident polarization to be selectively rotated. After the half-wave plate the beam is incident on an angled linear polarizer which only transmits the component of the beam with polarization parallel to the polarizer. Therefore, in principle the transmitted pulse energy can be tuned across its entire incident energy in principle. While this method is good for quick control, it is not effective in fine tuning the energy. More precise control of the pulse energy is done with a neutral density filter wheel (as shown in Figure 4.5) with a neutral density filter range of 0.0–2.4 in increments of 0.1. This setup therefore allows for the determination of micro-particle removal thresholds of individual micro-particles (the process of which is discussed in Section 4.2.2).

4.2 Experimental Techniques

The previous sections of this chapter have already discussed the design and equipment used to perform the experiments. It certainly is also important to cover the

methods used. The techniques used in this work essentially break into three areas: the preparation of the samples, the removal of the micro-particles and also, the final analysis of the samples.

4.2.1 Materials and Preparation

The micro-particles that were used consisted of two types of materials: dielectric and metallic micro-particles. With the dielectric materials it was possible to get micro-spheres but the metallic particles were irregularly shaped. The dielectric micro-spheres used were 2.5 μm (diameter) and 5.0 μm glass spheres from Duke Scientific and 2.2 μm poly-divinylbenzene (PDVB) spheres acquired from Harald Stöver at McMaster University. The metal micro-particles were 0.3 μm, 1 μm and 2 μm silver micro-particles which were acquired from Howard D. Glicksman at DuPont. The silver particles were also reported to have an organic layer surrounding them but the exact composition of this layer is unknown. The thickness of the layer was reported to be thin. Only the polymer micro-spheres were prepared prior to use; they were baked at around 300 °C in a vacuum oven in order to remove any solvents on their surface (the solvents being a possible result from the polymer micro-sphere creation process). The other micro-particles were used exactly as they had been received.

The types of substrates that were used cover the three basic types of materials: dielectrics (insulators), semiconductors and metals. A Corning glass cover slide was used for the dielectric substrate. Both single-crystal silicon and indium phosphide substrates were used for the semiconductors and a gold-coated iron substrate was used to represent a metal substrate. The skin depth of 800 nm light in gold is approximately 30 nm, so a gold layer with a thickness of approximately 100 nm was deposited to effectively have absorption of all the transmitted light from the surface occur in the coating. All of the surfaces were examined to check their smoothness

since rough surfaces can affect micro-particle binding forces. The semiconductor surfaces were very smooth (as can be seen in Figure 5.5) and the glass surface was also extremely smooth as shown in Figure 4.6(a). The gold surfaces did not show the same smoothness (see Figure 4.6(b)) and was a concern. The roughness of the gold surfaces was not an artifact from the coating process, but rather from the preparation of the iron substrate.

All the substrates were cleaned prior to use in order to remove any solvents or unknown particles from the surface. For the dielectric and metal substrates the cleaning was performed in an ultrasonic bath. The substrates were submerged in—in order of use—an acetone, methanol and dichloromethane solvent and subjected to ultrasonic cleaning for approximately five minutes with each solvent. The substrates were then dried with a strong nitrogen gun. The semiconductor substrates were cleaned in the clean room facilities at McMaster University. They first were dipped into a 2% hydrogen fluoride solution for approximately two minutes and then bathed for ten minutes in warmed trichloromethane, acetone, methanol and isopropyl alcohol solvents. The substrates were then dried with a strong nitrogen gun. Some semiconductor substrates were cleaned in the same manner as the dielectrics and metals and the experimental results were found to be consistent.

The final step in preparing the samples was to deposit the micro-particles onto the substrate surfaces. The PDVB micro-spheres were the simplest to handle and were "poured" onto the surface. Due to their low density, shaking of the micro-sphere container resulted in a "gaseous fluid" which could be poured onto the surface. The particles then settled on the surface with an even spatial density. Unfortunately, the glass micro-spheres did not form this fluid and they had to be blown onto the surface using a Pasteur pipette and hand-bulb. The silver micro-particles tended to aggregate

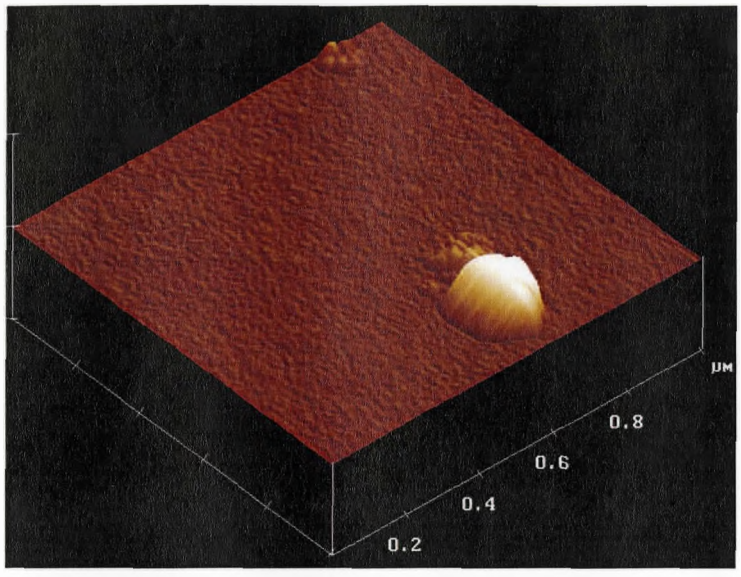

(a) Glass Substrate

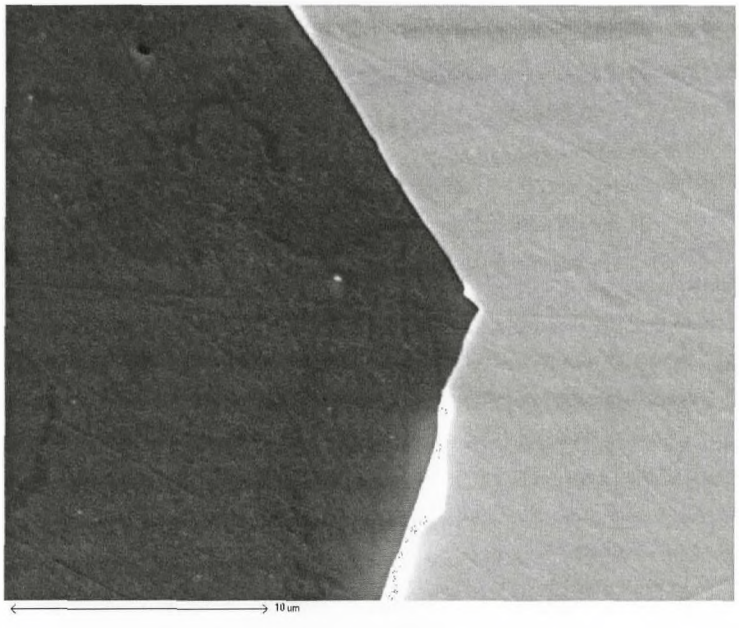

(b) Gold Substrate

Figure 4.6: Atomic force microscope and scanning electron microscope images of the (a) glass and (b) gold-coated iron substrates, respectively. The z-scale in (a) is 100 nm and shows (besides the large clump of contamination) a variation of the surface on the order of a couple of nanometers. In (b) both the gold coating (bright area) and the original iron (dark area) are visible. The surface striations can be seen on both the coating and the substrate.

together, and because of this they were simply dumped onto the surface. After a little bit of shaking, the particles were then dumped off the surface by rotating it. Individual particles did remain on the surface along with some micro-particle aggregates. After these processes for all the particles, any weakly bound micro-particles were removed by subjecting the surface to a strong air jet.

4.2.2 Micro-Particle Removal Process

Prior to removing the spheres the beam and the CCD camera have to be focussed onto the surface. The sample is placed on the mechanical stage and focussing is done simply by finding the lowest pulse energy which will machine the surface; in other words, the minimal fluence required to observe surface damage caused by the laser beam. This is done iteratively. Starting at a low pulse energy, the beam is scanned across a section of the substrate. The energy is gradually increased until surface damage is observed. At this point the pulse energy is decreased and the height of the objective is varied until damage is again seen. The pulse energy is again decreased and the process repeats itself until no more damage can be seen. It is at this point—when the minimum pulse energy causes damage—that the focus of the beam is on the surface. To determine the position of the focus along the surface a single shot is used to create a small crater. The camera is focussed onto this spot and the cross-hairs are used to mark the beam center location.

The process used to determine the threshold for micro-particle removal starts with the targeting of an individual micro-particle. The Spitfire output is set to 10 Hz so individual pulses can also be selected. A high neutral density filter setting is chosen so that the pulse energy is much less than required for removal. An individual pulse is then selected by the shutter while watching the monitor for any micro-particle movement. If there is no movement, the neutral density filter setting is decreased

and the process repeated with a higher pulse energy. This will continue until particle movement is observed and the filter setting is recorded. This filter setting corresponds to the minimum pulse energy required to move this particular particle. Information on how far the particle is moved is also obtained and falls into two categories: micro-particles that come to rest inside the field of view of the camera and those that are not seen after removal. After one micro-particle was observed to move after irradiation, another is targeted and the above process is repeated. In this way, statistics of the pulse energies required for removal of micro-particles from the surface are obtained and a threshold for removal can be determined.

From the recorded neutral density filter settings it is possible to determine the pulse energy and fluence. To make this conversion the beam power was measured just before the neutral density filter wheel using a standard optical power meter. Pulse energies can then be determined from the beam power and pulse repetition rate. To determine the electromagnetic field intensities, the pulse length must be known and was measured using an autocorrelator described above. The pulse energy (E), average fluence ($\mathcal{F}_{av}$) and average intensity (I_{av}) at the beam focus are then determined through the equations

$$E = E_o 10^{-x}, \tag{4.3}$$

$$\mathcal{F}_{av} = \frac{E}{\pi\omega_o^2}, \tag{4.4}$$

$$I_{av} = \frac{\mathcal{F}_{av}}{\tau_p}, \tag{4.5}$$

where E_o is the incident pulse energy, x the ND filter wheel setting and τ_p the pulse length. These expressions give the average values for the pulse intensity and fluence, but for the current situation the peak values are more appropriate. This is because the beam waists used were around 5 microns while the micro-particle sizes were around 2

microns. Since the particle is located in the center of the beam profile and is roughly a fifth of the beam waist, the pulse intensity or fluence the particle experiences is best represented by the peak values and not the average values. The peak values can be determined from the average values by multiplying the averages by two. To show that this is true we first look at the equation

$$F_{av}\pi\omega_o^2 = F_{peak}\int_0^{\infty}\int_0^{2\pi} re^{-2r^2/\omega_o^2}d\theta dr. \tag{4.6}$$

The left hand side of this equation is the expression for the total energy for a pulse with a top hat intensity profile. The right hand side is the expression for the total energy for the same pulse with a Gaussian intensity profile. The total energy of the pulse is the same and equating the two expressions allows a relationship between the average fluence and peak fluence (F_{peak}) to be determined. Solving Equation (4.6) in terms of the peak fluence gives

$$F_{peak} = 2F_{av}. \tag{4.7}$$

There is one final correction that must be made to the measured pulse values. Measurement of the beam power prior to the ND filter wheel and near the focal spot of the beam results in a difference. This is due to energy losses at the different optical components and it should be accounted for. The loss is estimated by taking the ratio of the two values (generally around 85%) and multiplying Equations (4.3) to (4.5) by this value. It is through this method that the peak threshold fluence for micro-particle removal is determined.

4.2.3 Post-Experiment Analysis

For some samples the surfaces were examined using a scanning electron microscope (SEM) or an atomic force microscope (AFM) after particle removal. Since these are well-established techniques, only a few points about their operation that affected

these results will be mentioned. The operation of a SEM relies on electron emission from the material surface. A beam of electrons is focussed into a spot on the surface which results in the emission of electrons. The emitted electrons are then detected and an electrical signal is produced proportional to the number of detected electrons. The electron beam focus can then be scanned across the surface and an image is formed. The images produced allow for the characterization of surface features, but no quantitative data is produced. One aspect in the effectiveness of a SEM is the conductivity of the sample. If it is insulating, charging of the surface occurs and the images become distorted. While the surface can be coated with a conducting material, an AFM may also be used to image the surface. In this method the force between a sharp tip and the surface is used to image the surface. Qualitative data on the surface variation is determined by measuring the deflection of the probe tip.

One problem in this post-analysis was finding where the spheres had been removed from. In order to locate these positions, a box or circle was machined around the removal area. This size of these surface marks ranged from around 40 μm to about 150 μm. This allowed the removal region to be easily found on the surface, and it also helped in determining if any features on the surface could be attributed to the removal process. Screen captures from the monitor prior to removal also allowed the position of removed micro-particles to be found accurately.

Chapter 5

Experimental Results and Discussion

In the previous chapters the theoretical and experimental background behind this work was presented. It is finally in this chapter that this development is put to the test. The majority of the research on dry laser cleaning with short pulses has involved nanosecond lasers. More recently, a European group has started to look at the removal of micro-particles using femtosecond lasers [7,9] but have only examined dielectric micro-particles on silicon and glass substrates. In the current work their experiments have been repeated as well as expanded on. The removal of dielectric and metal micro-particles from dielectric, semiconductor and metal substrates has been examined.

This chapter begins with a quick overview of some early experiments that were performed and led to the current body of work. From this more historical perspective of the work's development, attention is turned to the experimental results for the material combinations that were explored. Finally, the experimental results are discussed and trends are highlighted in terms of the parameters varied and subsequent dominant removal mechanism.

5.1 Early Experiments

This initiative started with some early observations made by Jan Thøgersen and Andrzej Borowiec. They deposited polymer micro-sphere arrays on surfaces and noticed the removal of micro-spheres during femtosecond pulse irradiation. The experiments were simply preliminary; the surfaces were neither cleaned prior to removal nor examined after removal. However, these experiments did prove to be the initial impetus for the present work.

From these observations it was initially believed that the light forces may be responsible for the removal of the micro-spheres. Because of this, early efforts were made by myself and Henry Tiedje to determine the actual magnitude of this force on the micro-spheres. In doing this a Paul trap was employed. A Paul trap is a three-dimensional electronic trap for charged particles. While an electrostatic field cannot trap charged particles in three dimensions, an alternating electric field can successfully trap the particles. There is a stable point in the center of the trap and deviation from this point results in increasing force on the particle. The force exerted on the particle—and the ability of the Paul trap to confine particles—depends on the charge-to-mass ratio of the particle. Based on this, it was hoped that micro-spheres could be charged, trapped and irradiated with the femtosecond pulses and their deflections measured to give the magnitude of the light force.

In implementing the Paul trap experiments several problems were encountered. One had to do with properly charging the micro-spheres. Both triboelectric and corona charging of the spheres were attempted, but it was only some large, irregularly shaped particles that were successfully trapped. An experiment was performed using these particles because we believed that, though the particles were not spheres, the light force produced would represent an order of magnitude value for a true micro-

sphere. In this experiment the beam was not targeted directly on the micro-particle, but was located nearby. It was not until a high pulse energy was used that movement of the particle was observed. After irradiation it came to rest in a different position in the trap. This would be due to a change in the charge-to-mass ratio of the micro-particle. The change in the charge-to-mass ratio of the particle indicates that ionization of the surrounding air is occurring and the particle is capturing some of the produced free charge. This result highlighted an experimental consideration to us. First, charging of the micro-particles may occur leading to an electrostatic force. This meant that, for the Paul trap experiments to continue, the trap would have to be placed in a vacuum if the light force were to be measured over a range of pulse energies.

The main experimental efforts of this work related to removal of micro-particles from substrates. There were some early experiments that were performed in this regard. One such experiment was a comparison of the micro-particle removal threshold fluences for a sample in air and a sample in a vacuum. This was performed to see if air plays a role in the removal. The results showed that the removal thresholds were the same in both air and vacuum environments. A similar experiment that was performed by Henry Tiedje and Andrzej Borowiec involved setting up an electric field across the sample. This was done so that any charging of the micro-sphere would result in an electrostatic force. This force would then affect the removal thresholds and trajectories of any removed micro-particles. Their preliminary efforts in this regard resulted in no observable differences and likely indicates that micro-particle charging is not a major concern.

Some other early experiments also involved varying the properties of the pulse. The pulse length was varied and the removal threshold of PDVB micro-spheres from

a silicon substrate were measured for 120 fs, 260 ps and 10 ns pulses. The result of increasing the pulse length is an increase in the removal threshold. SEM scans of the surfaces after irradiation show ablation pits for the femtosecond and picosecond pulses, but for the nanosecond no well-defined pits are observed. However, it did appear that there were some subtle features on the surface and they may indicate that melting occurred. If this is the case, it would effect the applicability of using nanosecond lasers in the dry laser cleaning application since the substrate is damaged. Wavelength variations of the pulse were also briefly examined and showed that the longer the wavelength, the larger the removal threshold. As well, the microscope objectives used were varied. This resulted in different beam waists. The experiments mentioned so far all used a 10x objective, but it was determined that a 5x objective should be used to reduce beam–particle alignment issues (the 5x microscope objective results in a larger beam waist). Comparison of the removal thresholds for both objectives showed that the threshold fluences do not change when the beam waist changes.

5.2 Micro-Particle Removal Experiments

It was the experience and knowledge gained in the early experiments that led to experiments which will be discussed in this section. The experiments which will be discussed here were performed to determine the threshold peak fluence for the removal of various types of micro-particles from several types of substrate surfaces. This data, along with post-irradiation analysis of the surfaces, can help determine the mechanism that is responsible for micro-particle removal at pulse fluences near the threshold. The experiments were performed several times to check that the results were consistent. Only a single experimental "run" is presented for each experiment

and shows the variation of the peak threshold fluence. The results are presented in terms of the substrate that was used.

5.2.1 Dielectric Substrates

Most dielectric materials are transparent to visible and near-UV light. It is also possible to find dielectric materials that have an index of refraction that is similar to air. These qualities are interesting because they indicate that a high percentage of light incident onto the substrate will be transmitted through the substrate. So, if a thermal removal mechanism were to dominate the removal near the threshold, the pulse's energy would have to be primarily absorbed through a high-order process such as multi-photon absorption. One might expect then that a non-thermal mechanism will be responsible for micro-particle removal. Another interesting result of the similarity of the materials' index of refraction is that surface reflectivity will be low. Therefore, the free space calculations performed on the electromagnetic fields around a micro-sphere should be reasonable. In the current work a Corning glass cover slide substrate was used which has an index of refraction of approximately 1.5. This means that there is a reflection of approximately 4% of the incident light (for normal incidence) and the rest is transmitted through the substrate (provided multi-photon effects are not significant).

Both the glass and PDVB micro-spheres were removed from this substrate and histograms of the measured removal fluences are shown in Figure 5.1. As was mentioned in Section 4.2.2, pulses with increasing fluence are used to irradiate the surface until micro-particle movement is observed. The pulse fluence is controlled by neutral density filters and the data collected in terms of the number of times micro-spheres were first observed to move with a given ND filter setting. The ND filter settings are converted to pulse fluences through knowledge of the pulse energy.

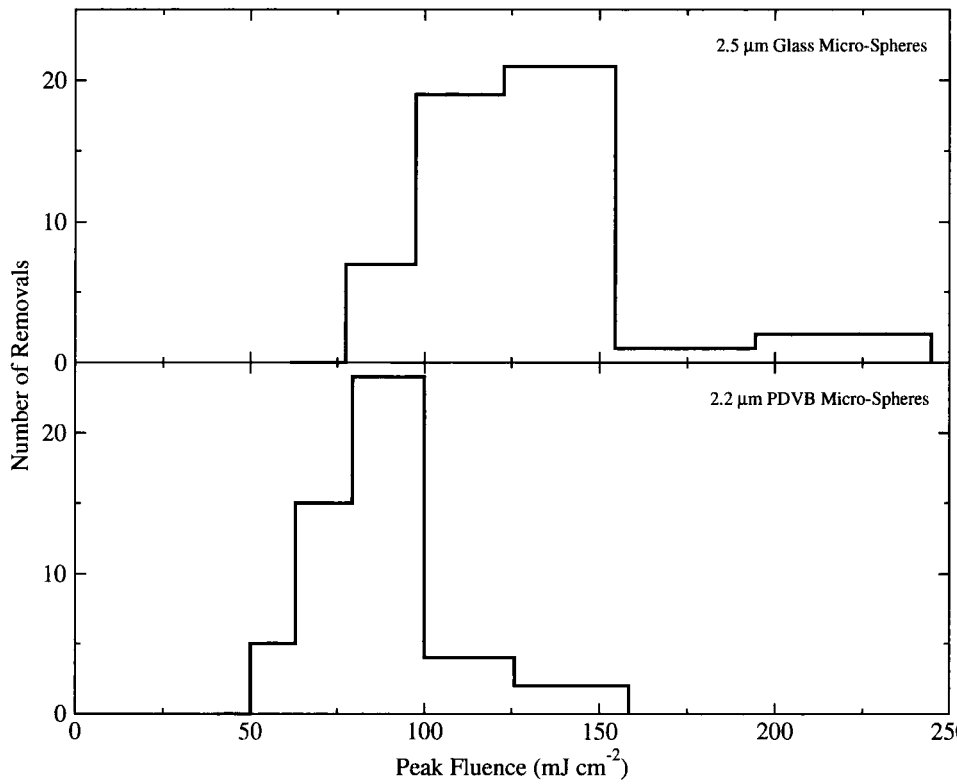

Figure 5.1: Histograms of the minimum peak fluences required to remove dielectric micro-spheres from a Corning glass cover slide. The x-axis corresponds to the minimum fluence required to remove a micro-sphere and the y-axis is the number of removed micro-particles that were observed. Therefore, the height of a histogram bar represents the number of micro-particles which had a minimum peak fluence required for removal. The width of the bar represents the range where the minimum peak fluence would be. In both graphs a total of 50 micro-spheres were removed with a pulse length of approximately 170 fs.

Therefore, the x-axis of the graph corresponds to the minimum energy required to move the micro-particles and the y-axis corresponds to the number of micro-particles that were observed to move within a given range of fluences (dictated by the width of the histogram bars). What the graph tells us about the relation between pulse fluence and micro-particle removal is at fluences below the histogram bars there will be no removal, but at fluences above the histogram bars there will be removal of all the micro-particles. In the region within the histogram bars there is no guarantee

that, at a given fluence, 100% of the particles irradiated will be removed. A piece of recorded information related to the removal that has not been included in Figure 5.1 is the distance the micro-particles were removed. In some cases this distance was large (outside the monitor's field of view which is around 100 μm) and in others it was small (within the monitor's field of view and could range from several microns to around 100 μm), but the removal distance was never consistent for a given fluence. However, there does seem to be a trend where at smaller fluences the removal distance is more often short and within the field of view of the viewing camera. Likewise, at higher fluences the removal distance is more often outside the camera's field of view.

Some comments should also be made about the histogram bars themselves. The histogram bars are not placed symmetrically around the observation points (i.e. the fluences where micro-particle removals were examined). The bars are drawn between the observation points. This is done is such a way that the width of the bars correspond to the fluence region in which the removals occurred. For example, suppose a given number of micro-particles were removed at a ND filter setting of 1. Since the fluence is controlled in ND filter setting steps of 0.1, this would mean that these micro-particles were not removed at a filter setting of 1.1. However, the critical filter setting for removal could be between 1.0 and 1.1 and thus, the histogram bar is drawn between 1.0 and 1.1 to represent this. The ND filter settings are transformed into fluences and plotted accordingly. This also highlights why the histogram bars vary in width. The steps occur in sizes of 0.1 and the pulse fluence is related to the filter setting (x) by

$$F \propto 10^{-x}. \tag{5.1}$$

This means the width of the bars will increase with increasing fluence (decreasing filter setting).

In Figure 5.1 there is a variation in the peak removal fluences that were observed. This may be due to a variety of causes. One cause of the variation would be due to a difference in micro-particle sizes. For example, the glass micro-spheres have a mean size of 2.5 μm and a standard deviation of 0.5 μm. This variance of the particle size can affect the binding forces as well as the electromagnetic fields around the micro-particle. Assuming a van der Waals binding force, which varies linearly with the particle size, there should be around a 20% variation in the binding force. According to the free-space electromagnetic field enhancements, a 2.0 μm glass micro-sphere would result in a 35 times enhancement of the incident field whereas a 3.0 μm micro-sphere would give a 84 times enhancement (a 2.5 μm micro-sphere gives a 51 times enhancement). Therefore, for a 3.0 μm glass micro-sphere, there is a 63% increase in the maximum intensity on the substrate surface when compared with the 2.5 μm micro-sphere. This can account for the dispersion of observed peak removal fluences. There can also be other effects and one of which would be due to local irregularities of the micro-particle or surface. They can be either of a physical nature where protrusions or indentations of the surfaces leads to different binding forces, or it may be of a chemical nature which can lead to differences in binding energies or other properties which effect the removal process. As well, particle–beam misalignment may effect the observed removal fluences, but these effects have been minimized by choosing the 5x microscope objective, which increases the beam spot size. One final note to be made with regard to the micro-particle removals is that it was an "all or nothing" process, or in other words there was no observable effect due to irradiating a micro-particle multiple times. Tests were performed where a particle was irradiated with a near-threshold pulse and if removal was not observed after the first shot, multiple pulses were applied to the micro-particle. In all cases the micro-

particles either were removed one the first pulse, or never (up to 15–20 pulses were applied to the micro-particles). Therefore, cumulative damage or incubation does not seem to be occurring, at least on a scale that results in removal of the micro-particles.

The graphs give the variation of the minimum fluence required to remove the micro-particles. From this data, a threshold peak fluence for removal (F_{th}) is determined as the mean of the values given by

$$F_{th} = \frac{1}{N}\sum_i F_i, \tag{5.2}$$

where N is the total number of removals and F_i is the fluence where the i^{th} removal occurred. The standard deviation (σ) of the data is also determined and calculated using

$$\sigma^2 = \frac{1}{N-1}\sum_i (F_i - F_{th})^2. \tag{5.3}$$

The standard deviation gives a measure of the width of the removal fluence variation. Using these equations the threshold for 2.5 μm glass micro-sphere on a Corning glass substrate is 110(25) mJ cm^{-2} (the number in the brackets corresponds to the standard deviation). For the 2.2 μm PDVB micro-spheres on the same substrate the threshold is 75(17) mJ cm^{-2}.

Examination of the glass surface after glass and polymer micro-sphere removal was attempted with a SEM. Since Corning glass is non-conducting, a gold layer had to be sputter-coated onto the surface prior to SEM imaging. No evidence of any surface features were found. However, it was unknown whether the gold coating would hide anything that might be created by the removal process. We were then motivated to look for features using an AFM partly because Münzer *et al.* had observed "pits" left after irradiation of 800 nm polystyrene spheres on a glass substrate [7]. The first time this was attempted the area that needed to be scanned for any features was too

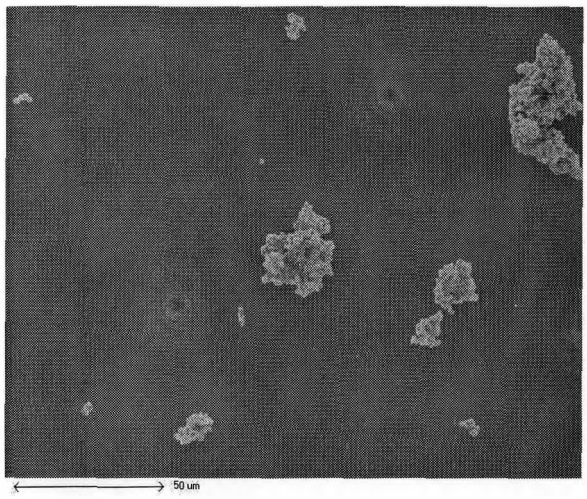

Figure 5.2: An example of the silver micro-particles on a silicon substrate. The majority of deposited particles are clusters. Several small clusters are visible, as well as one individual micro-particle that was not removed.

large and nothing was found. This could either be due to the lack of any real features being produced, or it may be a result of the large area of the scan.

The removal of the silver micro-particles for the glass substrate was also examined. Due to the aggregation of the particles it is very rare to find individual micro-particles. Therefore, good statistics of the removal fluences was not possible. However, several micro-particles which appeared not to be a micro-particle cluster were removed. Figure 5.2 is a SEM scan of a silicon substrate containing the silver micro-particles and it shows that aggregates are mainly formed on the surface. The peak fluence threshold for micro-particle removal in this case was 550(210) mJ cm^{-2} at a pulse length of approximately 140 fs. The large standard deviation is due to the relatively low number of micro-particles removed. This threshold is significantly higher than the corresponding thresholds for dielectric micro-particles. This would be expected for a thermal removal mechanism since the intensity enhancement would not be as large for the metallic micro-particle.

The ablation threshold for the Corning glass that was used for this work has not been determined. However, the ablation thresholds for similar transparent glass substrates was determined by Q. Liu using the same laser system. For BK7 glass the peak ablation threshold is 1 J cm^{-2} and for fused silica it is 2 J cm^{-2} [53]. The ablation threshold for the Corning glass substrate that was used is likely within the same region. Examining the field enhancements that were calculated, the glass micro-sphere could result in an enhancement factor of 51 (see Figure 3.2(c)), the PDVB micro-spheres in a factor of 47 (see Figure 5.8(c)) and the silver micro-particles in a factor of 5.0 (see Figure 3.6(c)). This would correspond roughly to fluences of 5.61 J cm^{-2}, 3.52 J cm^{-2} and 2.75 J cm^{-2} for the glass, PDVB and silver micro-particles respectively, and were calculated using the threshold fluences. All these values are greater than the substrate ablation threshold. However, this is also likely greater than the micro-sphere ablation thresholds. The ablation threshold of silver for a 120 fs pulse with a wavelength of 800 nm is approximately 400 mJ cm^{-2} [54]. The ablation thresholds for polymethylmethacrylate (PMMA) and polystyrene (PS) with 150 fs pulses at 800 nm are approximately 2.3 J cm^{-2} and 1.8 J cm^{-2}, respectively [55]. Again, the ablation threshold of PDVB is likely within this same region. These thresholds seem to indicate that ablation will be responsible for the micro-particle removal; it just remains a question of where the ablated material comes from. Based on the research of Münzer *et al.* with PS micro-spheres on BK7 glass [7], it seems likely that substrate ablation is occurring for the dielectric micro-spheres. For glass, a comparison of threshold fluences cannot be made with the work of Münzer *et al.* because they unfortunately did not publish this data.

5.2.2 Semiconductor Substrates

The semiconductors that were examined offer optical properties that differ from the dielectrics used. Both silicon and indium phosphide substrates were used and their respective band gaps are less then the energy of a 800 nm photon. Therefore, the absorption of the pulse energy can occur through a single photon and the higher intensities which drive multi-photon absorption are not needed. The surface reflectivities are also greater than the dielectric case and will have a greater effect on the electromagnetic fields around the micro-particles. Besides these properties, the removal of micro-particles from semiconductors might well be of the most interest to industrial laser cleaning applications. In this section, the data pertaining to the removal of dielectric and metal micro-particles from silicon and indium phosphide substrates is presented.

Histograms of the minimum removal peak fluences for both the PDVB and glass micro-spheres on a silicon substrate are shown in Figure 5.3. Calculation of the threshold for the glass micro-spheres gives a value of 10(5) mJ cm^{-2} and for the PDVB micro-spheres this value is 14(5) mJ cm^{-2}. These values agree with the results of Mosbacher *et al.*, who record a threshold of 11 mJ cm^{-2} for 1700 nm PS micro-spheres from silicon [9]. After irradiation, the silicon surfaces were easily imaged using a SEM and the results of this for PDVB micro-spheres are shown in Figure 5.5(a). As is seen in the figure, there is obviously pitting of the substrate. This clearly indicates that ablation of the substrate is responsible for the PDVB micro-particle removal. For the glass micro-spheres the intensity enhancement is nearly the same as for the polymer and the removal threshold is also the same. This indicates that substrate ablation will also be responsible for the glass micro-sphere removal.

The removal of the dielectric micro-spheres was also examined on an indium

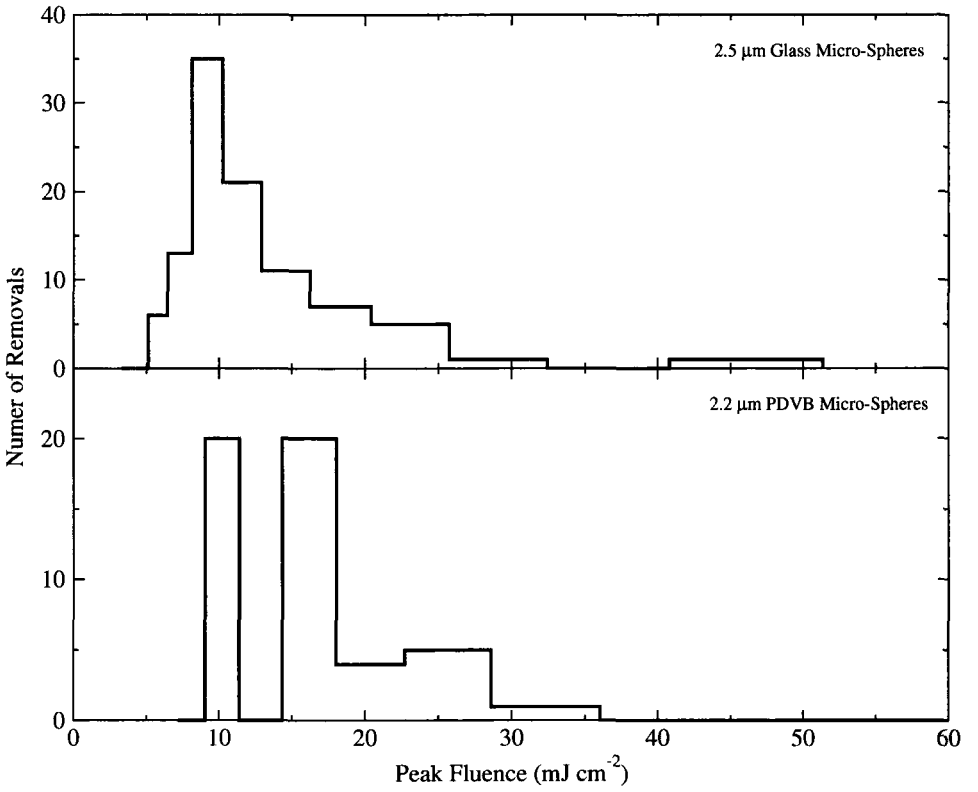

Figure 5.3: Histograms of the minimum peak fluences required to remove dielectric micro-spheres from a silicon substrate. In the top graph a total of 100 micro-spheres were removed with a pulse length of approximately 140 fs. In the bottom graph a total of 50 micro-spheres were removed with a pulse length of approximately 150 fs.

phosphide substrate. The peak fluence removal histograms are shown in Figure 5.4. The peak removal threshold for the glass micro-spheres is 7(2) mJ cm^{-2} and for the PDVB micro-spheres it is 6(1) mJ cm^{-2}. Pitting of the indium phosphide surface after the removal of PDVB micro-spheres can also be seen in Figure 5.5(b) and the dimensions of the pit are approximately the same as the silicon pit. Due to the similarity of the removal thresholds and intensity enhancements for the glass and PDVB micro-spheres, ablation is expected to occur under a glass micro-sphere as well. The ablation thresholds of silicon and indium phosphide surfaces for 120 fs pulses at a wavelength of 800 nm are 300 mJ cm^{-2} and 160 mJ cm^{-2}, respectively [56,57]. This

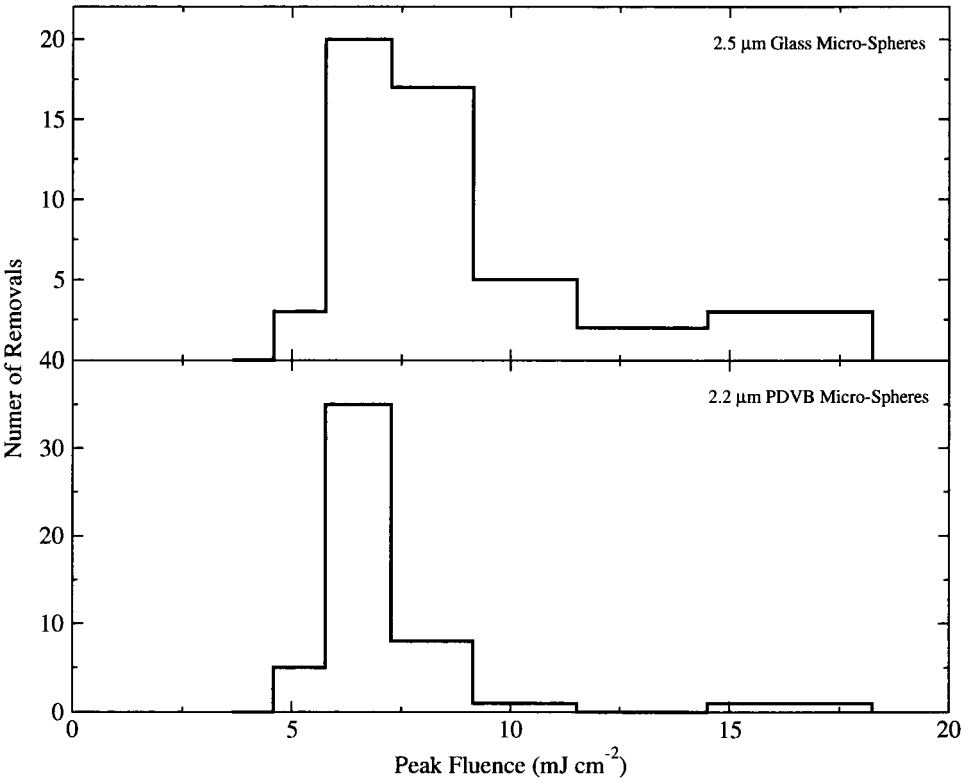

Figure 5.4: Histograms of the minimum peak fluences required to remove dielectric micro-spheres from a indium phosphide substrate. In both graphs a total of 50 micro-spheres were removed with a pulse length of approximately 140 fs.

gives an ablation threshold ratio of silicon to indium phosphide of approximately 2:1 which can also be seen in the micro-sphere removal threshold ratio. If the intensity enhancements are also evaluated it would result in intensities of 510 mJ cm^{-2} and 470 mJ cm^{-2} below the glass and PDVB micro-spheres on the silicon substrate, respectively. On the indium phosphide substrate the intensities would be approximately 310 and 280 mJ cm^{-2} for the glass and PDVB micro-spheres. The enhancement would certainly result in fluences above the substrate ablation thresholds, but in this case they would be below the micro-sphere material ablation thresholds. This indicates—as well as the 2:1 ratio of the removal thresholds—that ablation of the substrate is responsible for dielectric micro-sphere removal from absorbing semiconductor sub-

strates.

The removal of silver micro-particles from silicon and indium phosphide substrates was also examined. Again, there were problems with the aggregation of the micro-particles and good statistics of the peak fluences for removal were hard to achieve. But for both substrates more than ten micro-particles were removed and from this data thresholds were determined. For the silicon substrate the threshold is 245(81) mJ cm^{-2} and for the indium phosphide substrate the threshold is 133(14) mJ cm^{-2}. After irradiation the silicon surface was examined with a SEM and no pits were observed. This may mean that ablation is not occurring. However, it could be argued that ablation is still responsible for the removal. The Si and InP removal thresholds show approximately a 2:1 ratio that was discussed in terms of the dielectric micro-spheres. The removal thresholds are also very close to the substrate ablation thresholds. Any enhancement of the incident field could certainly result in ablation. The result of this is the indication that ablation is occurring, but why were no pits observed in the SEM? The answer could rely on two reasons. When depositing the micro-particles there are very few particles that actually stick to the surface. Most of these adhered micro-particles are actually aggregates and therefore, wide areas need to be examined for only several removed micro-particles (this can be seen in Figure 5.2). This means that the actual locations of the removed micro-particles are hard to determine. As well, it is unknown what the size of any pits would be and, therefore, they could be nearly undetectable with the resolution of the SEM. An AFM could image smaller details on the surface but the area which can be scanned becomes smaller. With an AFM the determination of the location of removed micro-particles becomes even harder. Despite the lack of SEM or AFM evidence of substrate ablation, the removal threshold results for silver micro-particles on semiconductor substrates do

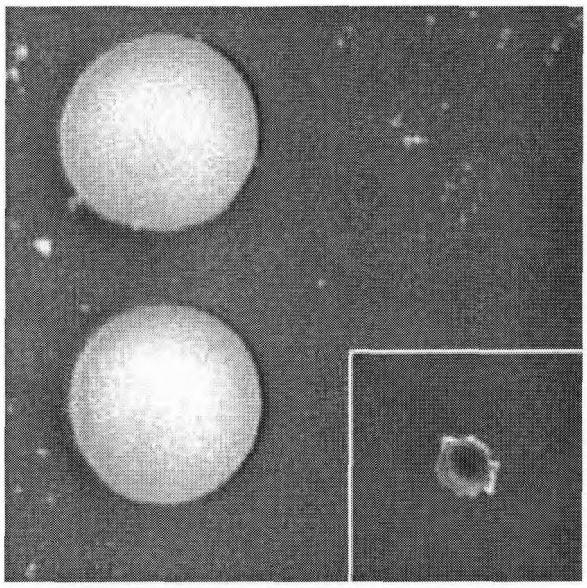

(a) Silicon

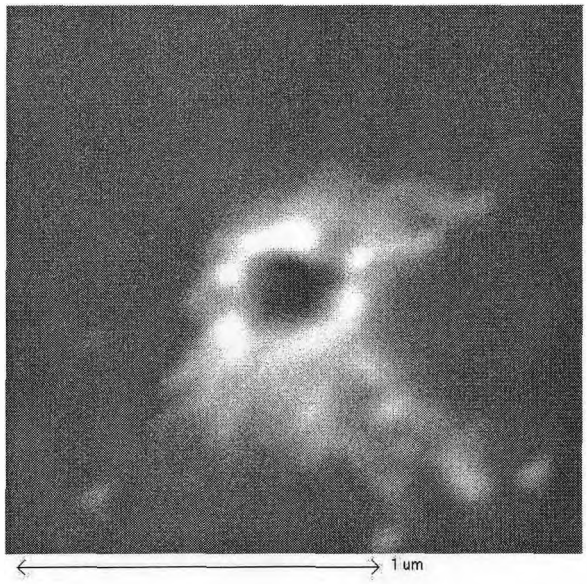

(b) Indium phosphide

Figure 5.5: SEM images of semiconductor substrates after 2.2 μm PDVB microparticle removal. Ablation craters can be clearly seen for both substrates. The diameters of the craters are around 400–500 nm.

imply that substrate ablation is the responsible removal mechanism.

5.2.3 Metal Substrates

The last type of material substrate examined was a metal. A metal will absorb electromagnetic energy without requiring high intensities to drive multi-photon absorption. This is similar to the behaviour of the semiconductors and the wavelength of light used in this work, but with a metal there usually is also a high surface reflectivity. For gold at 800 nm the normal incidence reflectivity is 98.6% [18]. As well, the transmitted light is absorbed in a very thin layer below the surface. Therefore, this material provides a substrate with optical properties different from the others already studied and may seriously affect the electromagnetic fields around the micro-particles. In this work, the only metal substrate examined was a gold-coated iron substrate.

On the gold substrate the only dielectric micro-particles examined were the glass micro-spheres. The peak removal fluence histogram is shown in Figure 5.6 and the calculated threshold is 36(16) mJ cm^{-2}. After irradiation, the surface was examined with a SEM and no definite pits were observed. However, for a micro-sphere that was removed at a fluence of approximately 150 mJ cm^{-2}, there was a pit and it is shown in Figure 5.7. This pit is similar to the pits on semiconductors in terms of size and shape, and it is obvious in this particular case that ablation was responsible for the removal. What is not so clear is the cause of removal near the threshold. The ablation threshold for gold using 100 fs pulses at a wavelength of 1053 nm is 450 mJ cm^{-2} [58] and at 800 nm the threshold would be similar. The removal threshold is significantly lower than the ablation threshold and the intensity enhancement which would have to be produced by the micro-sphere is roughly 10-15 times the incident intensity. Even with the large amount of light reflected by the surface this intensity enhancement may be possible. What may be occurring near the removal threshold

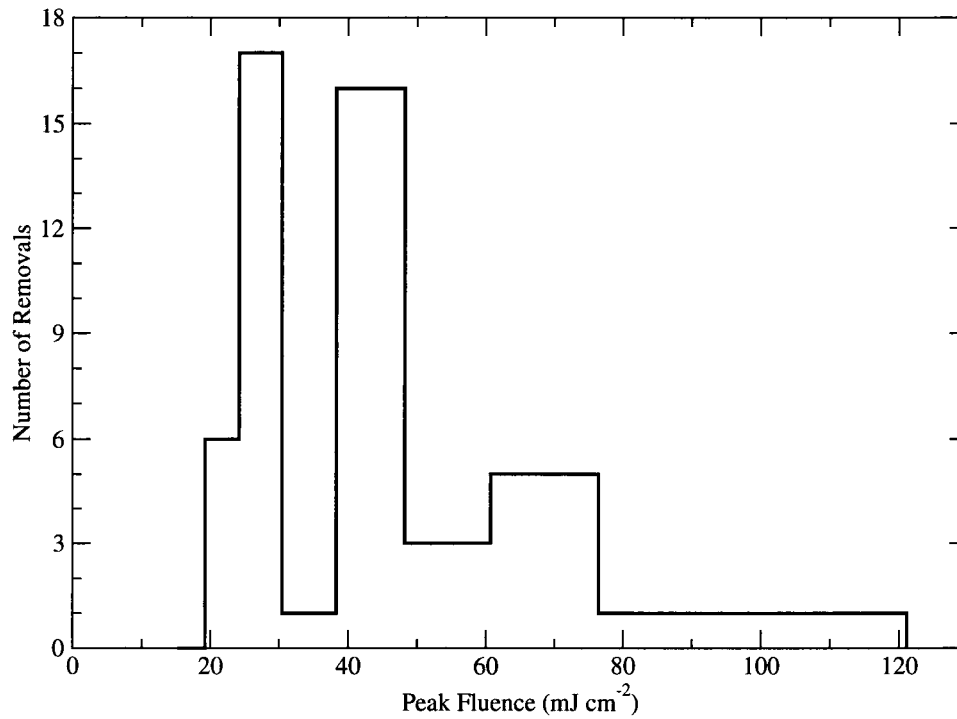

Figure 5.6: Histogram of the minimum peak fluences required to remove glass micro-spheres from a gold substrate. In the graph a total of 50 micro-spheres were removed with a pulse length of approximately 140 fs.

is that only a small amount of material is boiling off the surface resulting in pits which are very hard to observe in the SEM. However, it is not entirely clear what is responsible for the removal of the glass micro-spheres.

The removal of silver micro-particles from the gold substrate was observed as well. A large number of removals were not done due to the aggregation of the metal micro-particles. The data did give a peak fluence removal threshold of 800(110) mJ cm^{-2} and again the surface was examined with a SEM after irradiation. No ablation pits were observed but problems locating the region where the removals took place were encountered. However, in this case there is a significant pulse fluence above the particle which could either result in particle or substrate ablation. As in the glass substrate case, the removal threshold is larger than the actual bulk silver ablation

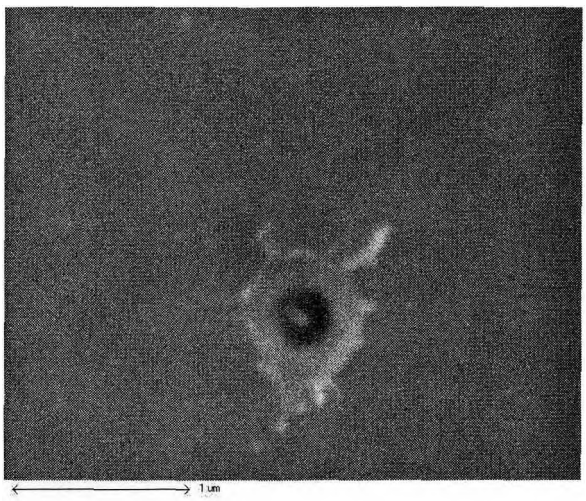

Figure 5.7: SEM image of a gold substrate after 2.5 μm glass micro-particle removal. Ablation craters can be clearly seen when a peak pulse fluence of 150 mJ cm^{-2} was used (this is significantly higher than the removal threshold). The diameter of the crater is around 400 nm.

threshold and makes particle ablation a possibility. As well, the removal threshold is larger than the substrate ablation threshold and ablation could occur on the surface. Based on this, it is expected that ablation is responsible for the micro-particle removal but it is not certain where the ablation is occurring.

5.3 Summary of Results

So far the results have been presented in a fashion where they were organized by the substrate used in the experiment. Most of the discussion has also just pertained to the removal of a certain micro-particle from a certain substrate and the broader trends and comparisons have not been examined. In this section these broader issues will be presented. This is basically done through an discussion of the summarized results presented in Table 5.1.

We first examine the results of the dielectric micro-spheres. It was evident that the removal of PDVB micro-spheres from the semiconductor substrates occurred

Micro-Particle	Substrate			
	Corning Glass	Silicon	Indium Phosphide	Gold
2.5 μm Glass	110(25)	10(5)	7(2)	36(16)
2.2 μm PDVB	75(17)	14(5)	6(1)	–
2.0 μm Silver	550(210)	245(81)	133(14)	800(110)

Table 5.1: Comparison of the peak fluence thresholds (in mJ cm^{-2}) for micro-particle removal from substrates. The thresholds are given as the mean of the minimum removal thresholds observed and the standard deviation of the data is given in the brackets.

because of substrate ablation. The observation of ablation pits below the removed micro-particles was not singular to this work alone. Similar work [7, 9] has shown the same pitting for polymer micro-particles on silicon substrates. The pits are also reported to occur at the same laser fluences observed by us. Substrate ablation will also lead to glass micro-sphere removal from semiconductors. This conclusion comes from two observations in Table 5.1. The first observation is that the removal thresholds for both glass and polymer micro-spheres are the same and the intensity enhancements beneath both types of spheres are also very similar (see Figure 5.8). The second observation is the 2:1 ratio of the removal thresholds for either the glass or polymer micro-spheres from the two semiconductor substrates; this is also the ratio of the substrate ablation thresholds. The removal of the dielectric micro-spheres from the glass substrate is expected to be due to ablation since the intensity enhancements can produce surface intensities large enough for ablation. However, in this case the removal threshold of PDVB is slightly lower than the glass threshold. The case of glass micro-spheres on a gold substrate does not give conclusive evidence for ablation. The intensity enhancements could lead to ablation based on the measured threshold, but pits on the surface were not observed. However, in comparing the removal thresholds for all the different substrates, it does appear that the substrate is responsible for

micro-particle removal and that removal would occur though a thermal mechanism. The removal thresholds of the absorbing substrates are lower than the non-absorbing substrate. Dielectric micro-spheres are removed from semiconductors at the lowest fluence, and this is followed by the metal and then the dielectric substrates. This is the same ordering as the ablation thresholds and the ratios between the fluences are roughly the same. This indicates that ablation is likely responsible for the removal of the dielectric micro-particles from the substrate surfaces examined.

The removal of the silver micro-particles were not as easy to characterize. This is mainly due to their nature when deposited on the substrate: the locations of the removed particles were not easy to find. As well, a large number of particles could not be removed since most of the deposited micro-particles aggregated together. However, we still were able to determine the removal thresholds on all the substrates. The removal thresholds for the two semiconductor substrates showed the 2:1 ratio of the ablation thresholds. As well, the removal thresholds were only slightly less than the ablation thresholds. Therefore, only a slight enhancement of the incident pulse would be required for substrate ablation and this is responsible for the micro-particle removal. The removal thresholds on the glass and gold substrates are quite high. The fluences could result in ablation of the substrate—a little enhancement would be needed for the glass substrate but the removal threshold on gold is greater than gold's ablation threshold—but they are also high enough to result in ablation of the micro-particle. It is therefore expected that removal of silver micro-particles from the substrates examined was facilitated by ablation.

A final note on the validity of the calculated electromagnetic fields is that the calculated enhancements do not match with the ratio of the removal and ablation thresholds. This would be expected since the effect of the different types of material

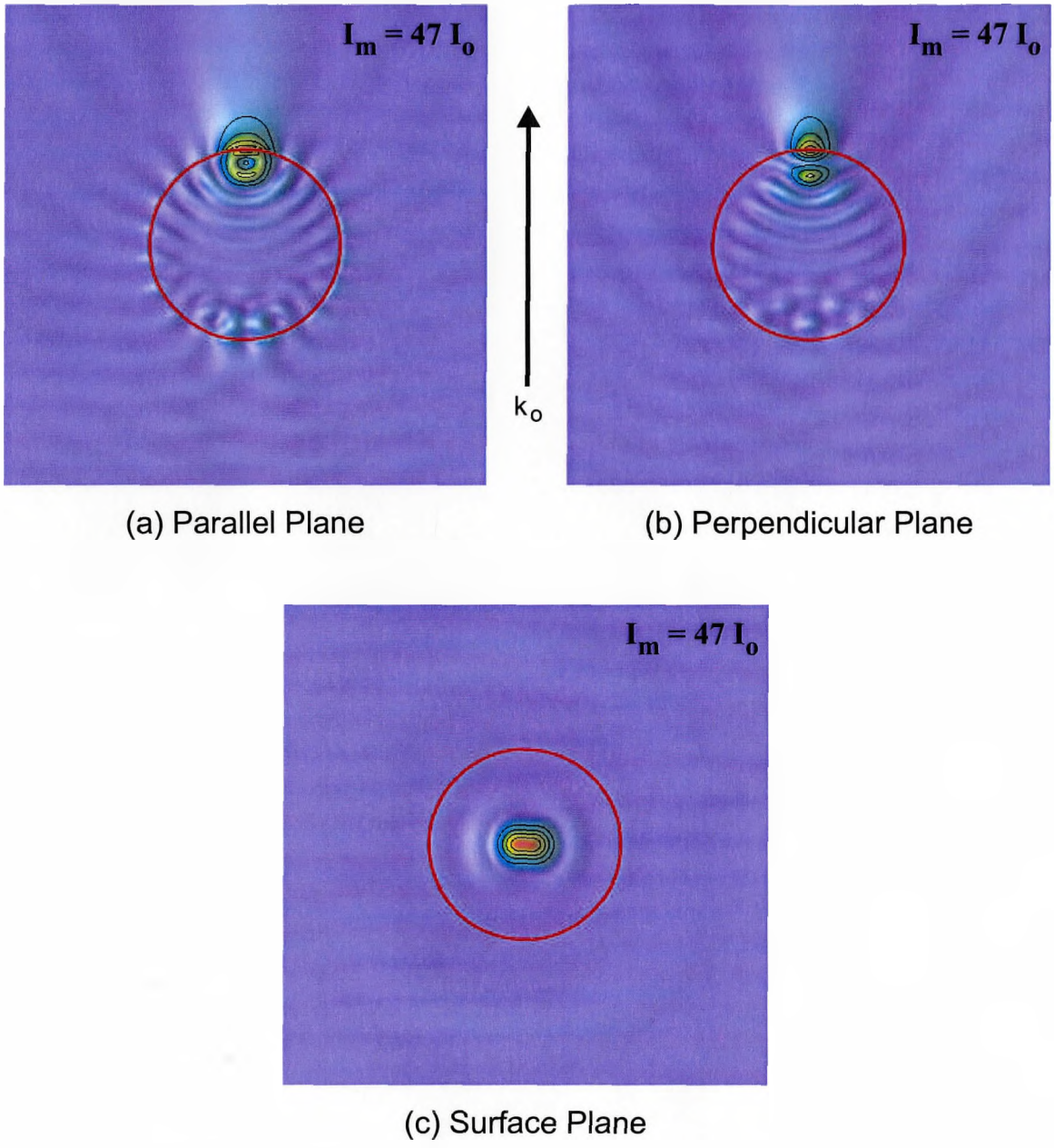

Figure 5.8: Intensity distributions for a 2.2 μm polydivinylbenzene micro-sphere. The intensity enhancement for this sphere is very close to the enhancement for a 2.5 μm glass micro-sphere. The contour interval for all the figures is $10I_o$.

surfaces was neglected in the calculations. As well, there may be other effects on the enhancements due to particle deformation or laser beam properties. However, the calculated results do not differ greatly from what might be determined from the experimental results. The required experimental enhancements are still roughly within a factor of two from the calculated ones.

Chapter 6

Conclusion

With the current development of technology the manipulation and modification of materials on the nano- and micro-meter size scale is starting to become important. Just as the reasons for doing this are varied, the methods of manipulation can also come in a variety of forms. One intriguing method of micro-manipulation is through the use of lasers. In the past, optical traps (commonly referred to as *optical tweezers*) have been used, and are still being used, to hold and move micro-sized objects [59]. Optical tweezers have used c.w. lasers but it might be possible to do the same thing with ultrafast lasers given the right conditions. Or the use of ultrafast lasers might open up new alternatives which don't exist for c.w. lasers. It was questions like this that fed the curiosity behind the currently reported work. In order to understand how to control the manipulation of micro-particles, it is necessary to determine the nature of the interaction between the ultrashort pulses and particles. It was attempted to measure the light force directly in a Paul trap, but then the focus turned to the interaction of the pulses with particles on surfaces. This study has mainly evaluated the interactions in terms of their ability in removing the particles from the surfaces. However, a wide variety of other manipulation possibilities may exist.

From this work it appears that the micro-particle removal is facilitated through

ablation when using femtosecond pulses. The local electromagnetic field enhancements are predominantly the reason leading to ablation. This is certainly true in the case of dielectric micro-spheres; the *focussing powers* of the two examined micro-spheres are nearly the same which results in similar removal thresholds. This removal threshold also lies below the substrate ablation thresholds and for semiconductor substrates ablation pits were directly observed. For the other substrates no pits were observed, but this is believed to be primarily due to pragmatic problems in locating and imaging any features. The intensity enhancement calculations certainly predict peak fluences below the micro-spheres which are greater than the substrate ablation thresholds. In the case of the silver micro-particles, the calculated enhancement by these micro-particles should result in removal thresholds close to the ablation thresholds. This too was observed with the semiconductor and metal substrate removal thresholds equaling the removal thresholds and for the glass substrate, the removal threshold was nearly equal to the glass ablation threshold. However, with the silver micro-particles, it is also possible that the particle itself is ablating material.

Several possible removal mechanisms were discussed in Chapter 2 but they haven't been addressed since. The reason is because they are not responsible for the experimental observations. One such mechanism relates to light forces. They were quickly dismissed as playing a role since the energy imparted to the particle would be very small even though the force is large. This may not be the case if the experimental conditions were changed. If the pulses were brought in at a quick repetition rate, it might be possible to manipulate the particles due to the continual application of the light force. Ionization was also presented as a removal mechanism but in the current situation it does not play a significant role. Perhaps the strongest evidence of this is due to the similarity of the glass and polymer micro-sphere removal thresh-

olds. Optically the materials are similar, but chemically they are quite distinct. This likely means that they have different rates of ionization which would lead to different removal thresholds by ionization. A similar argument would exist for the silver micro-particles. As well, the existence of shock waves was presented as a possible mechanism behind the removal of micro-particles. This is not occurring since the removal of a targeting micro-sphere did not result in the removal of micro-spheres located nearby. In some cases the closest micro-sphere was only around 10 μm away from the removed sphere and it is likely that any shock wave which was produced would affect other particle located within a region comparable to several particle diameters. This would mean that a shock wave significant enough to remove the micro-sphere did not exist. The final mechanism to discuss is material expansion which is reported to be responsible for removal with nanosecond pulses. It is not expected that this plays a role for a femtosecond pulse. If it is responsible for removal using nanosecond pulses is hard to know from this work. Some preliminary experiments performed by us with nanosecond pulses demonstrated that some large, shallow features were left on the surface and the work of Mosbacher *et al.* [9] indicated that melting occurs. These results suggest that micro-particle enhancement of the pulse can render the use of short laser pulses in dry laser cleaning applications undesirable.

The results of this work should not indicate that ablation would always be the dominant method of micro-particle removal. There still remains a large parameter space that can be explored. One such parameter is the laser wavelength. Provided the index of refraction does not change too much, longer wavelengths make the size parameter smaller and for shorter wavelengths the opposite is true. For dielectric particles, the decreased size parameter would mean that the intensity enhancements are smaller and it is possible that other interactions may dominate. For metal parti-

cles, the intensity enhancements increase and ablation becomes more likely. Different wavelengths could also affect the nature of absorption and this would be most pronounced when using semiconductors. If the photon energy were lowered below the band gap energy of the semiconductor, multi-photon absorption would have to occur. As well, the wavelength might be tuned to elicit a resonance response of the materials used (for example, phonon resonances). The laser pulse lengths may also be changed. While this might affect all the removal mechanisms, this might be the most advantageous for the light forces because the force will act on the particle longer. This is advantageous because for removal of the micro-particle, the energy imparted to it would be larger resulting in a more effective removal. Other possibilities involve the redesign of the removal setup. For example, the pulses could be incident on the surface at an angle.

As was mentioned in the introduction, there are numerous applications for the manipulation of micro-particles. One application that is quite readily applied to the current work is laser cleaning. Under the examined experimental conditions the use of ultrafast lasers might not be too promising. This is due to potential damage done to the surface. The validity of a cleaning mechanism would presumably depend on its ability to leave the surface undamaged, but if minor damage could be tolerated, then ultrafast lasers might be acceptable. Through the use of different beam configurations it might also be possible to clean surfaces without damaging them. If the beam were incident at an angle that is not perpendicular to the substrate the maximum enhancement would not lie on the surface. A related method has been employed by A. N. Karpetis *et al.* to clean the inside of cryostat windows using nanosecond pulses [60]. In their work the cryostat was filled with liquid helium and the inner side of the window was inaccessible but covered with particles. A nanosecond pulsed

laser beam was incident on the particles from outside the transparent window and the particles were removed. Light forces are presumably responsible for the removal since there is no intensity enhancement on the substrate. As reported by J.M. Lee *et al.*, the removal of the micro-particles using shock waves produced in air also appears to be a promising method of removal [35]. These techniques correspond to dry laser cleaning, but another method of wet laser cleaning [61] could also be effectively employed with ultrafast lasers. In this method a layer of liquid is applied to the surface prior to removal. The change in the external index of the micro-particle would result in smaller intensity enhancements while the energy delivered to the surface would remain roughly the same. In this manner it is possible that ablation would not occur. Even though the conditions used in the current work indicate that the substrates are damaged in the removal, there are still viable possibilities in cleaning surfaces with ultrafast lasers.

In terms of future directions this research could take, one obvious route is through another promising application of manipulation of micro-particles using ultrafast lasers. This would lie in micro-patterning where regular arrays of micro-particles could be deposited on the substrate and subsequently removed. This would result in regular arrays of ablation pits. Preliminary work in this regard has been carried out by H.-J. Münzer *et al.* [7], but they did not actually create regular micro-sphere arrays. Spatial patterning of micro-particles on surfaces has been examined before [62–64] using either laser beam patterning or aqueous suspension deposition and in reference [64] the substrate was subsequently patterned using argon ion beams. The use of ultrafast lasers could ultimately be advantageous over this method since a laser would be more cost effective and much easier to incorporate into the apparatus. This certainly could be one future direction that would be easily carried out under the

current experimental setup. Laser cleaning could also be further evaluated by exploring the effects of angular cleaning and varied pulse length on different materials. The light forces could be further explored by using dielectric micro-spheres which have significant non-linearities. This non-linear component of the light forces could significantly change the removal mechanism. On a somewhat theoretical side, it would be interesting to develop the enhancement programs to include the substrate. This could lead to interesting electromagnetic field distributions where the particles can be manipulated without damaging the surface. Whatever the future directions may turn out to be, there is plenty of parameter space to explore which may lead to interesting and important results.

Appendix A

Mie Theory Fields

The Mie theory expressions for the incident, internal and scattered electromagnetic fields are:

INCIDENT FIELD

$$
\begin{aligned}
E_r^i &= e^{\imath k^{(I)} r\cos\theta}\sin\theta\cos\phi \\
E_\theta^i &= e^{\imath k^{(I)} r\cos\theta}\cos\theta\cos\phi \\
E_\phi^i &= -e^{\imath k^{(I)} r\cos\theta}\sin\phi \\
H_r^i &= \frac{\imath k^{(I)}}{k_2^{(I)}} e^{\imath k^{(I)} r\cos\theta}\sin\theta\sin\phi \\
H_\theta^i &= \frac{\imath k^{(I)}}{k_2^{(I)}} e^{\imath k^{(I)} r\cos\theta}\cos\theta\sin\phi \\
H_\phi^i &= \frac{\imath k^{(I)}}{k_2^{(I)}} e^{\imath k^{(I)} r\cos\theta}\cos\phi
\end{aligned}
$$

INTERNAL FIELD

$$
\begin{aligned}
E_r^w &= \frac{\cos\phi}{(\tilde{k}^{(II)}r)^2}\sum_{l=1}^{\infty} l(l+1)\,{}^e\tilde{A}_l\psi_l(\tilde{k}^{(II)}r)P_l^1(\cos\theta)\\
E_\theta^w &= -\frac{\cos\phi}{\tilde{k}^{(II)}r}\sum_{l=1}^{\infty}\left[{}^e\tilde{A}_l\psi_l'(\tilde{k}^{(II)}r)P_l^{1'}(\cos\theta)\sin\theta - \imath\frac{{}^m\tilde{A}_l\psi_l(\tilde{k}^{(II)}r)P_l^1(\cos\theta)}{\sin\theta}\right]\\
E_\phi^w &= -\frac{\sin\phi}{\tilde{k}^{(II)}r}\sum_{l=1}^{\infty}\left[\frac{{}^e\tilde{A}_l\psi_l'(\tilde{k}^{(II)}r)P_l^1(\cos\theta)}{\sin\theta} - \imath\,{}^m\tilde{A}_l\psi_l(\tilde{k}^{(II)}r)P_l^{1'}(\cos\theta)\sin\theta\right]\\
H_r^w &= \frac{\imath\sin\phi}{\tilde{k}^{(II)}k_2^{(II)}r^2}\sum_{l=1}^{\infty} l(l+1)\,{}^m\tilde{A}_l\psi_l(\tilde{k}^{(II)}r)P_l^1(\cos\theta)\\
H_\theta^w &= -\frac{\sin\phi}{\tilde{k}^{(II)}r}\sum_{l=1}^{\infty}\left[\frac{{}^e\tilde{A}_l\psi_l(\tilde{k}^{(II)}r)P_l^1(\cos\theta)}{\sin\theta} + \imath\,{}^m\tilde{A}_l\psi_l'(\tilde{k}^{(II)}r)P_l^{1'}(\cos\theta)\sin\theta\right]\\
H_\phi^w &= -\frac{\cos\phi}{k_2^{(II)}r}\sum_{l=1}^{\infty}\left[{}^e\tilde{A}_l\psi_l(\tilde{k}^{(II)}r)P_l^{1'}(\cos\theta)\sin\theta + \imath\frac{{}^m\tilde{A}_l\psi_l'(\tilde{k}^{(II)}r)P_l^1(\cos\theta)}{\sin\theta}\right]
\end{aligned}
$$

SCATTERED FIELD

$$
\begin{aligned}
E_r^s &= \frac{\cos\phi}{(k^{(I)}r)^2}\sum_{l=1}^{\infty} l(l+1)\,{}^e\tilde{B}_l\tilde{\xi}_l(k^{(I)}r)P_l^1(\cos\theta)\\
E_\theta^s &= -\frac{\cos\phi}{k^{(I)}r}\sum_{l=1}^{\infty}\left[{}^e\tilde{B}_l\tilde{\xi}_l'(k^{(I)}r)P_l^{1'}(\cos\theta)\sin\theta - \imath\frac{{}^m\tilde{B}_l\tilde{\xi}_l(k^{(I)}r)P_l^1(\cos\theta)}{\sin\theta}\right]\\
E_\phi^s &= -\frac{\sin\phi}{k^{(I)}r}\sum_{l=1}^{\infty}\left[\frac{{}^e\tilde{B}_l\tilde{\xi}_l'(k^{(I)}r)P_l^1(\cos\theta)}{\sin\theta} - \imath\,{}^m\tilde{B}_l\tilde{\xi}_l(k^{(I)}r)P_l^{1'}(\cos\theta)\sin\theta\right]\\
H_r^s &= \frac{\imath\sin\phi}{k^{(I)}k_2^{(I)}r^2}\sum_{l=1}^{\infty} l(l+1)\,{}^m\tilde{B}_l\tilde{\xi}_l(k^{(I)}r)P_l^1(\cos\theta)\\
H_\theta^s &= -\frac{\sin\phi}{k^{(I)}r}\sum_{l=1}^{\infty}\left[\frac{{}^e\tilde{B}_l\tilde{\xi}_l(k^{(I)}r)P_l^1(\cos\theta)}{\sin\theta} + \imath\,{}^m\tilde{B}_l\tilde{\xi}_l'(k^{(I)}r)P_l^{1'}(\cos\theta)\sin\theta\right]\\
H_\phi^s &= -\frac{\cos\phi}{k_2^{(I)}r}\sum_{l=1}^{\infty}\left[{}^e\tilde{B}_l\tilde{\xi}_l(k^{(I)}r)P_l^{1'}(\cos\theta)\sin\theta + \imath\frac{{}^m\tilde{B}_l\tilde{\xi}_l'(k^{(I)}r)P_l^1(\cos\theta)}{\sin\theta}\right]
\end{aligned}
$$

The $\tilde{A}$ and $\tilde{B}$ coefficients are determined from:

$$
\begin{aligned}
{}^{e}\tilde{A}_l &= \frac{\tilde{n}}{\psi_l'(\tilde{n}q)}\left[i^{l-1}\frac{2l+1}{l(l+1)}\psi_l'(q)+\tilde{\xi}_l'(q)\,{}^{e}\tilde{B}_l\right], \\
{}^{m}\tilde{A}_l &= \frac{\tilde{n}}{\psi_l(\tilde{n}q)}\left[i^{l-1}\frac{2l+1}{l(l+1)}\psi_l(q)+\tilde{\xi}_l(q)\,{}^{m}\tilde{B}_l\right], \\
{}^{e}\tilde{B}_l &= i^{l+1}\frac{2l+1}{l(l+1)}\frac{\tilde{n}\psi_l'(q)\psi_l(\tilde{n}q)-\psi_l(q)\psi_l'(\tilde{n}q)}{\tilde{n}\tilde{\xi}_l'(q)\psi_l(\tilde{n}q)-\tilde{\xi}_l(q)\psi_l'(\tilde{n}q)}, \\
{}^{m}\tilde{B}_l &= i^{l+1}\frac{2l+1}{l(l+1)}\frac{\tilde{n}\psi_l(q)\psi_l'(\tilde{n}q)-\psi_l'(q)\psi_l(\tilde{n}q)}{\tilde{n}\tilde{\xi}_l(q)\psi_l'(\tilde{n}q)-\tilde{\xi}_l'(q)\psi_l(\tilde{n}q)}.
\end{aligned}
$$

Bibliography

[1] W.D. Scharfe and W. Rath. Lasers for industrial applications in material processing. *Material Science Forum*, 301:253–286, 1999.

[2] J. Squier and M. Müller. High resolution nonlinear microscopy: A review of sources and methods for achieving optimal imaging. *Rev. Sci. Instrum.*, 72:2855–2867, 2001.

[3] S. Svanberg. Some applications of ultrashort laser pulses in biology and medicine. *Meas. Sci. Technol.*, 12:1777–1783, 2001.

[4] A. Ashkin. Acceleration and trapping of particles by radiation pressure. *Phys. Rev. Lett.*, 24:156–159, 1970.

[5] R. Omori, T. Kobayashi, and A. Suzuki. Observation of a single-beam gradient-force optical trap for dielectric particles in air. *Opt. Lett.*, 22:816–818, 1997.

[6] C.-B. Juang et al. Synthesis of nanometer glass particles by pulsed-laser ablation of microspheres. *Appl. Phys. Lett.*, 65:40–42, 1994.

[7] H.-J. Münzer et al. Local field enhancement effects for nanostructuring of surfaces. *J. Microsc.*, 202:129–135, 2000.

[8] Y.F. Lu, Y.W. Zheng, and W.D. Song. An energy approach to the modelling of particle removal by pulsed laser irradiation. *Appl. Phys. A*, 68:569–572, 1999.

[9] M. Mosbacher et al. Optical field enhancement effects in laser-assisted particle removal. *Appl. Phys. A*, 72:41–44, 2001.

[10] R.A. Bowling. A theoretical review of particle adhesion. In K.L. Mittal, editor, *Particles on Surfaces 1: Detection, Adhesion, and Removal*, pages 129–142. Plenum Press, 1988.

[11] J.H. de Boer. The influence of van der Waals' forces and primary bonds on binding energy, strength and orientation, with special reference to some artificial resins. *Trans. Faraday Soc.*, 32:10–38, 1936.

[12] H.C. Hamaker. The London–van der Waals attraction between spherical particles. *Physica*, 4:1058–1072, 1937.

[13] K. Krupp. Particle adhesion: Theory and experiment. *Advan. Colloid Interface Sci.*, 1:111–239, 1967.

[14] E.M. Lifshitz. The theory of molecular attraction between solids. *Soviet Phys. JETP*, 2:73–83, 1956.

[15] B.V. Derjaguin, V.M. Muller, and Yu.P. Toporov. Effect of contact deformations on the adhesion of particles. *J. Colloid Interface Sci.*, 53:314–326, 1975.

[16] D.S. Rimai et al. Particles on surfaces: Adhesion induced deformations. In *Unknown*, pages 1–31. Unknown, 2000.

[17] J. Brandrup, E.H. Immergut, and E.A. Grulke, editors. *Polymer Handbook*. John Wiley & Sons, fourth edition, 1999.

[18] D.R. Lide, editor. *CRC Handbook of Chemistry and Physics*. CRC Press, eighty-first edition, 2000.

[19] T. Tlusty, A. Meller, and R. Bar-Ziv. Optical gradient forces of strongly localized fields. *Phys. Rev. Lett.*, 81:1738–1741, 1998.

[20] R. Pobre and C. Saloma. Single Gaussian beam interaction with a Kerr microsphere: characteristics of the radiation force. *Appl. Opt.*, 36:3515–3520, 1997.

[21] Y.F. Lu, Y.W. Zheng, and W.D. Song. Laser induced removal of spherical particles from silicon wafers. *J. Appl. Phys.*, 87:1534–1539, 2000.

[22] J.M. Lee, K.G. Watkins, and W.M. Steen. Angular laser cleaning for effective removal of particles from a solid surface. *Appl. Phys. A*, 71:671–674, 2000.

[23] J.M. Lee and K.G. Watkins. Laser removal of oxides and particles from copper surfaces for microelectronic fabrication. *Opt. Express*, 7:68–76, 2000.

[24] J.M. Lee, C. Curran, and K.G. Watkins. Laser removal of copper particles from silicon wafers using UV, visible and IR radiation. *Appl. Phys. A*, 73:219–224, 2001.

[25] T. Fourrier et al. Laser cleaning of polymer surfaces. *Appl. Phys. A*, 72:1–6, 2001.

[26] A.C. Tam, W.P. Leung, W. Zapka, and W. Ziemlich. Laser-cleaning techniques for removal of surface particulates. *J. Appl. Phys.*, 71:3515–3523, 1992.

[27] Y.F. Lu et al. Removal of submicron particles from nickel–phosphorus surfaces by pulsed laser irradiation. *Appl. Surf. Sci.*, 120:317–322, 1997.

[28] Y.F. Lu et al. Wavelength effects in the laser cleaning process. *Jpn. J. Appl. Phys.*, 37:840–844, 1998.

[29] G. Vereecke, E. Rohr, and M.M. Heyns. Laser-assisted removal of particles on silicon wafers. *J. Appl. Phys.*, 85:3837–3843, 1999.

[30] N.A. Inogamov et al. Expansion of matter heated by an ultrashort laser pulse. *JETP Lett.*, 69:310–316, 1999.

[31] A. Cavalleri, K. Skolowski-Tinten, J. Bialkowski, and D. von der Linde. Time of flight mass spectroscopy of femtosecond laser ablation of solid surfaces. In C.R. Phipps, editor, *High-Power Laser Ablation*, volume 3343, 1998.

[32] D.S. Moore et al. Ultrafast nonlinear optical method for generation of planar shocks. *Appl. Phys. Lett.*, 78:40–42, 2001.

[33] K.T. Gahagan et al. Measurement of shock wave rise times in metal thin films. *Phys. Rev. Lett.*, 85:3205–3208, 2000.

[34] J. Lee, M.F. Becker, and J.W. Keto. Dynamics of laser ablation of microparticles prior to nanoparticle generation. *J. Appl. Phys.*, 89:8146–8152, 2001.

[35] J.M. Lee and K.G. Watkins. Removal of small particles on silicon wafer by laser-induced airborne plasma shock waves. *J. Appl. Phys.*, 89:6496–6500, 2001.

[36] G. Mie. *Ann. d. Physik*, 25:377, 1908.

[37] M. Born and E. Wolf. *Principles of Optics.* Pergamon Press, fifth edition, 1975.

[38] P.W. Barber and S.C. Hill. *Light Scattering by Particles: Computational Methods*, volume 2 of *Advanced Series in Applied Physics.* World Scientific, 1998.

[39] W.J. Wiscombe. Improved Mie scattering algorithms. *Appl. Opt.*, 19:1505–1509, 1980.

[40] J.P. Barton, D.R. Alexander, and S.A. Schaub. Internal and near-surface electromagnetic fields for a spherical particle irradiated by a focused laser beam. *J. Appl. Phys.*, 64:1632–1639, 1988.

[41] C. Girard et al. Generation of optical standing waves around mesoscopic surface structures: Scattering and light confinement. *Phys. Rev. B*, 52:2889–2898, 1995.

[42] C. Girard et al. Optical magnetic near-field intensities around nanometer-scale surface structures. *Phys. Rev. B*, 55:487–497, 1997.

[43] P.W. Milonni and J.H. Eberly. *Lasers.* Wiley-Interscience, 1988.

[44] C. Girard and A. Dereux. Near-field optics theories. *Rep. Prog. Phys.*, 59:657–699, 1996.

[45] O.J.F. Martin, A. Dereux, and C. Girard. Iterative scheme for computing exactly the total field propagating in dielectric structures of arbitrary shape. *J. Opt. Soc. Am. A*, 11:1073–1080, 1994.

[46] O.J.F. Martin, C. Girard, and A. Dereux. Generalized field propagator for electromagnetic scattering and light confinement. *Phys. Rev. Lett.*, 74:526–529, 1995.

[47] M. Paulus, P. Gay-Balmaz, and O.J.F. Martin. Accurate and efficient computation of the Green's tensor for stratified media. *Phys. Rev. E*, 62:5797–5807, 2000.

[48] M. Paulus and O.J.F. Martin. Light propagation and scattering in stratified media: a Green's tensor approach. *J. Opt. Sci. Am. A*, 18:854–861, 2001.

[49] M. Paulus and O.J.F. Martin. A fully vectorial technique for scattering and propagation in three-dimensional stratified photonic structures. *Opt. Quant. Electron.*, 33:315–325, 2001.

[50] C. Rulliére, editor. *Femtosecond Laser Pulses: Principles and Experiments.* Springer–Verlag, 1998.

[51] G. Keiser. *Optical Fiber Communications.* McGraw–Hill, third edition, 2000.

[52] G.P. Agrawal. *Nonlinear Fiber Optics.* Academic Press, 1995.

[53] Q. Liu. Femtosecond laser ablation of selected dielectrics and metals. Master's thesis, McMaster University, 2001.

[54] K. Furusawa et al. Ablation characteristics of Au, Ag, and Cu metals using a femtosecond Ti:sapphire laser. *Appl. Phys. A*, 69:S359–S366, 1999.

[55] S. Baudach, J. Bonse, J. Krüger, and W. Kautek. Ultrashort pulse laser ablation of polycarbonate and polymethylmethacrylate. *Appl. Surf. Sci.*, 154/155:555–560, 2000.

[56] A. Cavalleri et al. Femtosecond melting and ablation of semiconductors studied with time of flight mass spectroscopy. *J. Appl. Phys.*, 85:3301–3309, 1999.

[57] J. Bonse, J.H. Wrobel, J. Krüger, and W. Kautek. Ultrashort-pulse laser ablation of indium phosphide in air. *Appl. Phys. A*, 72:89–94, 2001.

[58] C. Momma, S. Nolte, B.N. Chichkov, F.V. Alvensleben, and A. Tünnermann. Precise laser ablation with ultrashort pulses. *Appl. Surf. Sci.*, 109/110:15–19, 1997.

[59] A. Ashkin. Applications of laser radiation pressure. *Science*, 210:1081–1088, 1980.

[60] A.N. Karpetis, C.M. White, and K.R. Sreenivasan. Laser wipers. *Phys. Rev. E*, 62:4421–4423, 2000.

[61] M. Mosbacher et al. A comparison of ns and ps steam laser cleaning of Si surfaces. *Appl. Phys. A*, 69:S331–S334, 1999.

[62] K. Sasaki et al. Laser-scanning micromanipulation and spatial patterning of fine particles. *Jap. J. Appl. Phys.*, 30:L907–L909, 1991.

[63] L.M. Goldenberg et al. Ordered arrays of large latex particles organized by vertical deposition. *Langmuir*, 18:3319–3323, 2002.

[64] F. Burmeister et al. Colloid monolayer lithography—a flexible approach for nanostructuring of surfaces. *Appl. Surf. Sci.*, 144–145:461–466, 1999.